The Astrophysical Journal, 886:1 (16pp), 2019 November 20 https://doi.org/10.3847/1538-4357/ab46c2

Electron Densities and Nitrogen Abundances in Ionized Gas Derived Using [N II] Fine-structure and Hydrogen Recombination Lines

Jorge L. Pineda[1], Shinji Horiuchi[2], Loren D. Anderson[3,4,5], Matteo Luisi[3,4], William D. Langer[1], Paul F. Goldsmith[1], Thomas B. H. Kuiper[1], Geoff Bryden[1], Melissa Soriano[1], and T. Joseph W. Lazio[1]
[1] Jet Propulsion Laboratory, California Institute of Technology, 4800 Oak Grove Drive, Pasadena, CA 91109-8099, USA; Jorge.Pineda@jpl.nasa.gov
[2] CSIRO Astronomy & Space Science/NASA Canberra Deep Space Communication Complex, P.O. Box 1035, Tuggeranong ACT 2901, Australia
[3] Department of Physics and Astronomy, West Virginia University, Morgantown, WV 26506, USA
[4] Center for Gravitational Waves and Cosmology, West Virginia University, Chestnut Ridge Research Building, Morgantown, WV 26505, USA
[5] Green Bank Observatory, P.O. Box 2, Green Bank, WV 24944, USA
Received 2019 May 28; revised 2019 September 11; accepted 2019 September 17; published 2019 November 13

Abstract

We present a method for deriving the electron density of ionized gas using the ratio of the intensity of the [N II] 205 μm line to that of hydrogen radio recombination lines (RRLs). We use this method to derive electron densities of 21 velocity components in 11 lines of sight through the Galaxy, including the Galactic center. We observed, at high spectral resolution, the [N II] 205 μm with the *Herschel*/HIFI and SOFIA/GREAT instruments and the RRLs with the Green Bank Telescope and the NASA Deep Space Network Deep Space Station 43 (DSS-43) telescope. We find typical electron densities between 8 and 170 cm^{-3}, which are consistent with those derived at low spectral resolution using the [N II] 205 μm/122 μm ratio with *Herschel*/PACS on a larger sample of sight lines in the Galactic plane. By matching the electron densities derived from the [N II] 205 μm/RRL intensity ratio and the [N II] 122 μm/205 μm intensity ratio, we derive the nitrogen fractional abundance for most of the velocity components. We investigate the dependence of the N/H ratio on galactocentric distance in the inner Galaxy ($R_{\rm gal} < 6$ kpc), which is inaccessible in optical studies owing to dust extinction. We find that the distribution of nitrogen abundances in the inner Galaxy derived from our data has a slope that is consistent with that found in the outer Galaxy in optical studies. This result is inconsistent with some suggestions of a flatter distribution of the nitrogen abundance in the inner Galaxy.

Key words: HII regions – ISM: abundances – ISM: clouds – local interstellar matter

1. Introduction

The ionized gas component of the interstellar medium (ISM) occupies a large volume in galaxies (Haffner et al. 2009). It is found in diffuse form as the warm ionized medium (WIM), and in denser forms in H II regions surrounding massive stars and in the ionized boundary layers of molecular clouds. The structure and kinematics of the ionized gas are a reflection of the radiative and mechanical feedback from massive stars. Stellar feedback has been suggested to play a fundamental role in the regulation of star formation in galaxies (e.g., Hopkins et al. 2014), which in turn drives galaxy evolution. Thus, the study of the structure and kinematics of the ionized gas is an important tool for characterizing the effect that stellar feedback has in the ISM and for determining the role of stellar feedback in the regulation of star formation in galaxies.

After massive stars form, they produce energetic photons that ionize their dense surroundings. As the ionized gas is not in pressure equilibrium with its surrounding neutral gas, H II regions expand with time. Because the ionizing photon flux of a star is relatively constant over its lifetime on the main sequence, the mass of gas that it ionizes is relatively constant. Thus, as an H II region evolves, it becomes larger and its volume density diminishes. Eventually, the neutral gas surrounding H II regions becomes porous, and ionizing photons escape into the diffuse ISM, as suggested by power-law decreases in RRL intensities surrounding H II regions (Luisi et al. 2016, 2019). This ionizing photon leakage, which is more prominent in giant H II regions, can ionize hydrogen over a larger volume surrounding H II regions and can play an important role in maintaining the diffuse WIM (Haffner et al. 2009). The evolution of the ionized gas in star-forming regions is thus characterized by the volume density of electrons (n_e), which varies by orders of magnitude during the lifetimes of H II regions, ranging from $>10^4$ cm^{-3} in ultracompact H II regions (Churchwell 2002) to $\lesssim$0.1 cm^{-3} (Cordes & Lazio 2002; Haffner et al. 2009) in the diffuse WIM. Mechanical feedback from massive stars, such as stellar winds and supernova explosions, will further influence the density structure of the ionized gas, creating features such as bubbles, shock fronts, filaments, pillars, globules, and clumps. Studying the density structure and kinematics of ionized gas over large areas is crucial for understanding the evolution of star-forming regions and the impact of star formation on the ISM of galaxies.

Nitrogen, the fifth most abundant element, has an ionization potential of 14.6 eV, and therefore emission from ionized nitrogen arises exclusively from the ionized gas component of the ISM. The far-infrared [N II] 205 and 122 μm fine-structure lines are therefore important tracers of the highly ionized low-density WIM, the extended envelopes of H II regions, high-density H II regions, and partially ionized boundary layers of photon-dominated regions (PDRs). Emission from far-infrared [N II] is widespread throughout the Galaxy as shown by *COBE* (Bennett et al. 1994). The far-infrared [N II] lines are among the most important tracers of Galactic ionized gas, as they are not affected by dust extinction, which greatly restricts the variety of environments that ionized gas tracers in the optical and near-infrared can explore.

Goldsmith et al. (2015) observed the [N II] 122 and 205 μm fine-structure lines along ~100 lines of sight (LOSs) using the PACS instrument on *Herschel*, which had insufficient spectral

resolution to resolve the lines, and so they could only derive integrated intensities. The excitation analysis of the [N II] 122 and 205 μm lines indicates that the emission, over the whole inner Galaxy, arises from regions with relatively large volume densities ($n_e \simeq$ 10–100 cm^{-3}), larger than those expected for the diffuse WIM ($\lesssim$0.1 cm^{-3}) but lower than those typical of compact H II regions (>5 $\times$ 10^3 cm^{-3}; Kurtz 2005). The frequency and extent of the density components found by Goldsmith et al. (2015) are inconsistent with them arising only from compact H II regions, suggesting the presence of a ubiquitous moderately dense ionized gas component in the plane of the Milky Way (Geyer & Walker 2018). The *Herschel*/PACS observations lack velocity information, and therefore the resulting electron densities could arise from multiple H II regions along the LOS, and thus the information of the distribution of ionized gas in the Galactic plane is incomplete in this data set. High spectral resolution observations of the [N II] lines are necessary to separate spatially overlapping gas components along the LOS and trace the kinematics of ionized gas. The HIFI instrument on *Herschel* and the GREAT instrument on SOFIA have recently enabled observations of the [N II] 205 μm line at high spectral resolution (Persson et al. 2014; Langer et al. 2016, 2017a). However, neither of these instruments could observe the [N II] 122 μm line for use with the [N II] 205 μm line in the excitation analysis.

Radio recombination lines (RRLs) are also tracers of the ionized gas observed with the [N II] 122 and 205 μm lines. They have been extensively used to characterize the properties of ionized gas regions (Brown et al. 1978). Early observations of hydrogen recombination lines were limited to bright and dense H II regions owing to the low sensitivity of radio telescopes at that time. Recent advances in radio spectrometer technology, however, have enabled efficient observations of RRLs by observing a large number of distinct transitions simultaneously, thus obtaining sensitive observations by stacking several RRL lines. These new techniques have allowed the study of RRL emission over a wider range of environments and the detection of satellite recombination lines such as those from helium and carbon (Balser 2006; Anderson et al. 2011; Alves et al. 2015; Luisi et al. 2017). The RRL lines provide an unambiguous determination of the emission measure (EM = $\int n_{\rm e} N({\rm H}^+) dl$, where $n_{\rm e}$ and $N({\rm H}^+)$ are the electron density and ionized hydrogen column density, respectively), which can be combined with [N II] 205 μm surveys done with *Herschel* and SOFIA to determine the electron density of ionized gas at high velocity resolution. [N II] and RRL lines together can be used to provide a more complete picture of the properties of ionized gas in star-forming regions.

In this paper, we present a new approach that uses spectrally resolved hydrogen recombination lines together with the [N II] 205 μm line to determine the electron density. We apply this method in 11 LOSs distributed in the Galactic plane observed with *Herschel*/HIFI and SOFIA in [N II] 205 μm and the DSS-43 and GBT telescopes in hydrogen RRLs. This paper is organized as follows. We describe the RRL and [N II] observations in our selected sample in Section 2. In Section 3, we discuss the method used to derive electron densities from the ratio of the RRL to the [N II] 205 μm lines. In Section 4 we discuss the derived electron densities in the selected LOSs. We finally list our conclusions in Section 5.

2. Observations

2.1. [N II] Observations

We observed 10 LOSs in the Galactic plane in the [N II] 205 μm line at high spectral resolution using the HIFI (de Graauw et al. 2010) instrument aboard the *Herschel Space Observatory* (Pilbratt et al. 2010). These LOSs are part of the GOT C+ survey (Langer et al. 2010; Pineda et al. 2013), and the [N II] observations were presented by Goldsmith et al. (2015) and Langer et al. (2016). The intensities were converted from antenna temperature ($T_{\rm A}^*$) scale to main-beam brightness temperature, $T_{\rm mb}$, by using a main-beam efficiency $\eta_{\rm mb}$ of 0.60 (Roelfsema et al. 2012, updates in HIFI Beam Release Notes 2014 October). The data were smoothed to a velocity resolution of 1 km s^{-1} in order to increase the signal-to-noise ratio. The FWHM width of the *Herschel*/HIFI beam corresponds to 15.″7 for the [N II] 205 μm line. The typical rms antenna temperature of this data set is $T_{\rm mb}$ = 0.1 K in a 1 km s^{-1} channel. For the diffraction-limited *Herschel* HIFI beam, this rms is equivalent to an uncertainty in the intensity of $\Delta I = 3 \times 10^{-9}$ W m^{-2} sr^{-1}.

We also included in our analysis the GOT C+ LOS, G030.0+0.0, that was observed with SOFIA/GREAT and presented by Langer et al. (2017b). The angular resolution of these observations is 20″. We converted from $T_{\rm A}^*$ to $T_{\rm mb}$ intensity scale using a main-beam efficiency of 0.66 (Röllig et al. 2016). The spectrum has an rms noise of 0.12 K in a 1 km s^{-1} channel.

The observed *Herschel* and SOFIA [C II] and [N II] spectra, together with RRL observations described below, are shown in Figure 1. We also list their integrated intensities in Table 1 and the results of a Gaussian decomposition in Table 6. There is general agreement among the velocities of [C II], [N II], and RRL components. There are, however, differences in the [N II]/RRL line ratio, which is a signature of different physical conditions along the LOS (see Section 4.1). These differences in the [N II]/RRL ratio in LOSs with multiple velocity components in a small velocity range, mostly seen in the intrinsically narrower [N II] lines, result in apparent velocity shifts between [N II] and RRL lines (e.g., G013.9+0.0). However, when decomposing the data in Gaussian components, we find a good correspondence between the [N II] and RRL velocity components even in these LOSs, confirming the assumption that they both trace the same ionized gas.

2.2. Hydrogen Recombination Lines

We used the DSS-43 telescope to observe five LOSs in our sample in the H91α and H92α hydrogen RRLs at 8.58482 and 8.30938 GHz, respectively, using the *X*-band receiver in the position-switching observing mode. The angular resolution of the DSS-43 at 8.420 GHz is 115.″2. We converted the data from an antenna temperature to a main-beam temperature scale using a main-beam efficiency of 0.78. Both lines were resampled to a common spectral grid and averaged together to increase the signal-to-noise ratio, with the H92α intensities scaled to correspond to those of the H91α lines.[6] We fitted a

[6] As seen in Equation (4), in LTE, the intensity of an RRL is proportional to the EM, the line width, and line frequency. Given that EM and Δv are intrinsic properties of the source, the intensities of two RRLs are related by the inverse of the ratio of their frequencies. In the case when LTE does not apply (Equation (8)), however, a dependence on electron density and temperature is introduced to the relationship between two line intensities. For lines with similar principal quantum number, n, this effect is negligible, and assuming LTE is appropriate. For larger Δn, however, NLTE effects need to be taken into account when scaling RRL intensities.

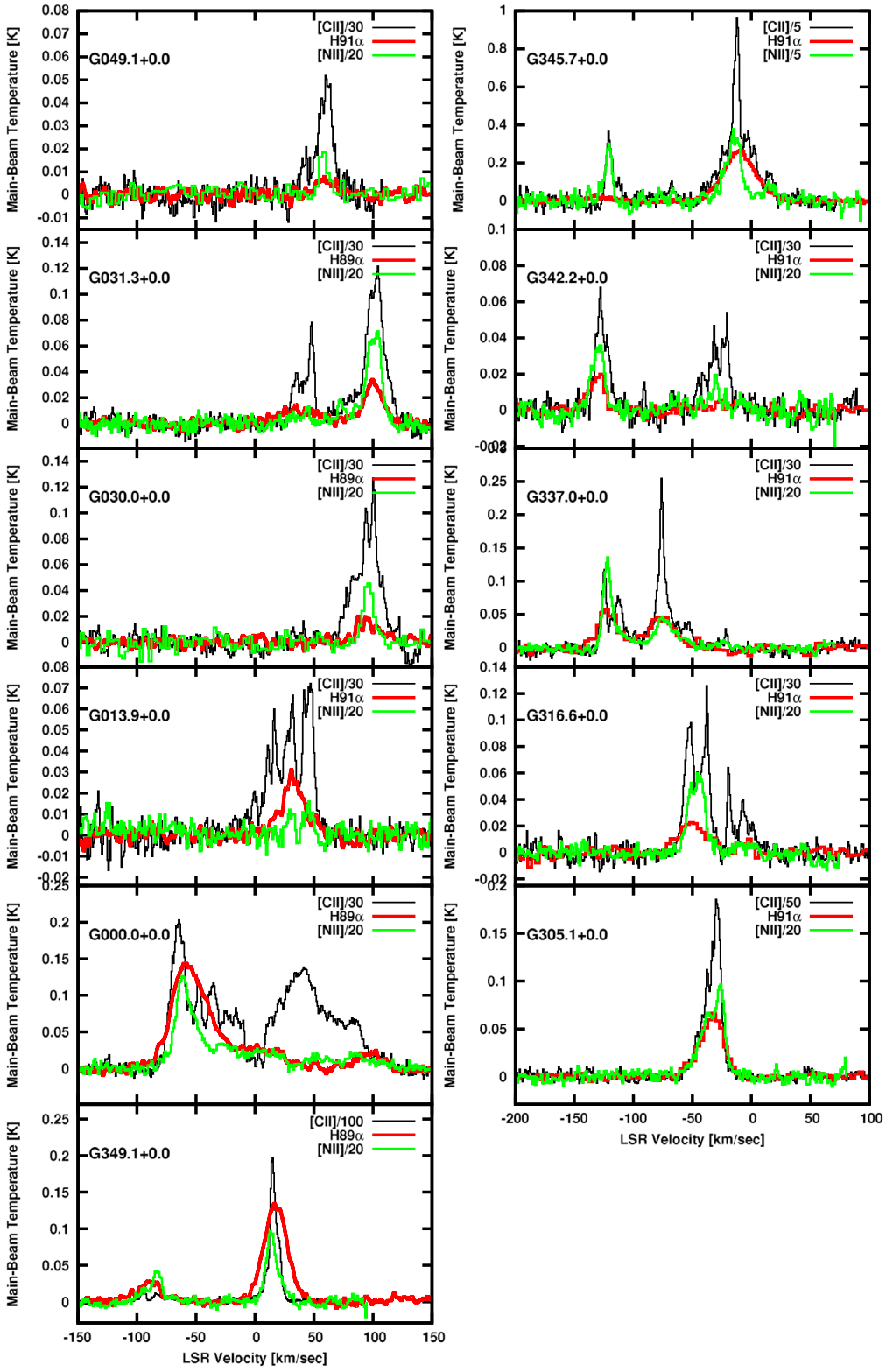

Figure 1. Observed spectra of [C II], [N II], and hydrogen recombination lines along the 11 LOSs in our sample.

polynomial baseline of order 3 to our data. The resulting spectra have a typical rms noise of 4 mK in a 1 km s^{-1} channel. We also used the DSS-43 telescope to observe the H67α (21.3846 GHz) at 47″ in the G345.7+0.0 LOS. We converted the spectrum from an antenna temperature to a main-beam temperature scale using a main-beam efficiency of 0.5, and we fitted a polynomial baseline of order 3. The spectra have an rms noise of 6 mK over the 3 km s^{-1} channel.

We also observed RRLs in six LOSs in our sample using the Versatile GBT Astronomical Spectrometer (VEGAS) on the Green Bank Telescope (GBT) in *X* band in the position-switching observing mode. The angular resolution of the GBT

Table 1
[N II] 205 μm and RRL Integrated Intensities[a]

LOS	l (deg)	b (deg)	V_{LSR} (km s^{-1})	I([N II]) 205 μm (K km s^{-1})	I(H91α) (K km s^{-1})	I(H89α) (K km s^{-1})	I(H67α) (K km s^{-1})	I(H54α) (K km s^{-1})
G305.1+0.0	305.106	0.0	−33.2	37.6 ± 0.9	1.58 ± 0.027[b]	⋯	⋯	⋯
G316.6+0.0	316.596	0.0	−48.1	20.9 ± 0.4	0.57 ± 0.027[b]	⋯	⋯	⋯
G316.6+0.0	316.596	0.0	−6.4	3.4 ± 0.4	0.12 ± 0.013[b]	⋯	⋯	⋯
G342.2+0.0	342.174	0.0	−131.2	9.7 ± 0.6	0.30 ± 0.021[b]	⋯	⋯	⋯
G337.0+0.0	336.957	0.0	−121.5	25.1 ± 0.5	1.13 ± 0.064[b]	⋯	⋯	⋯
G337.0+0.0	336.957	0.0	−76.6	21.3 ± 2.3	1.31 ± 0.080[b]	⋯	⋯	⋯
G345.7+0.0	345.652	0.0	−122.8	6.2 ± 0.4	0.35 ± 0.087[b]	⋯	⋯	⋯
G345.7+0.0	345.652	0.0	−8.2	16.2 ± 0.6	2.18 ± 0.010	⋯	0.89 ± 0.092[b]	⋯
G349.1+0.0	349.130	0.0	17.0	23.0 ± 0.8	2.25 ± 0.069	3.26 ± 0.014[b]	⋯	⋯
G349.1+0.0	349.130	0.0	−91.1	11.5 ± 0.9	0.73 ± 0.076	0.66 ± 0.007[b]	⋯	⋯
G000.0+0.0	0.000	0.0	−60.5	33.2 ± 1.7	4.251 ± 0.193	3.81 ± 0.018[b]	⋯	0.744 ± 0.073
G000.0+0.0	0.000	0.0	−37.1	45.7 ± 2.5	2.173 ± 0.204	2.40 ± 0.028[b]	⋯	⋯
G000.0+0.0	0.000	0.0	12.8	13.2 ± 2.3	0.516 ± 0.154	1.33 ± 0.019[b]	⋯	⋯
G000.0+0.0	0.000	0.0	95.0	14.8 ± 0.2	0.867 ± 0.118	0.70 ± 0.008[b]	⋯	⋯
G013.9+0.0	13.913	0.0	45.5	2.3 ± 0.3	⋯	0.14 ± 0.006[b]	⋯	⋯
G013.9+0.0	13.913	0.0	30.3	1.5 ± 0.3	0.373 ± 0.075	0.49 ± 0.006[b]	⋯	⋯
G030.0+0.0	30.000	0.0	95.4	10.2 ± 0.7	⋯	0.38 ± 0.030[b]	⋯	⋯
G031.3+0.0	31.277	0.0	100.4	20.9 ± 1.4	0.678 ± 0.197	0.63 ± 0.005[b]	⋯	⋯
G031.3+0.0	31.277	0.0	38.0	2.8 ± 0.9	⋯	0.51 ± 0.007[b]	⋯	⋯
G049.1+0.0	49.149	0.0	59.7	3.3 ± 0.3	0.078 ± 0.030	0.13 ± 0.004[b]	⋯	⋯

Notes.
[a] The intensities shown here are not corrected for beam-dilution effects (see Section 3.4).
[b] RRL intensities that are used in our analysis.

in X band is 84″. For each observed direction, we simultaneously measured seven H$n\alpha$ RRL transitions in the 9 GHz band, H87α to H93α, using the techniques discussed in Bania et al. (2010), Anderson et al. (2011), and Balser et al. (2011), and averaged all spectra together to increase the signal-to-noise ratio using `TMBIDL` (Bania et al. 2016). The data were resampled to a common grid, intensities were scaled to correspond to that for the H89α line (9.17332 GHz), and we averaged all lines in the band (two polarizations per transition) together to increase the signal-to-noise ratio. The GBT data weere calibrated using a noise diode of known power. The data were later corrected with a third-order polynomial baseline and smoothed to ∼1.9 km s^{-1}. We converted the intensities from an antenna temperature to main-beam temperature using a main-beam efficiency of 0.94. The typical rms noise of this data is 2.5 mK in a 1.9 km s^{-1} channel.

We also observed the H53α (42.95196 GHz) and H54α (40.63049 GHz) lines with the Q-band receiver on the GBT in the G000.0+0.0 LOS. These observations have an angular resolution of 16″, which is similar to that of the *Herschel* HIFI beam and can therefore be used to study beam-dilution effects. The spectra were averaged to increase the signal-to-noise ratio, with the H54α used as a reference. We converted the data from an antenna temperature to a main-beam temperature scale using a main-beam efficiency of 0.8, and we fitted a polynomial baseline of order 3. The spectra have an rms noise of 5 mK over the 1.1 km s^{-1} channel.

2.3. Sample Location with Respect to Known H II Regions

We studied the environment traced by our sample LOS by searching for the nearest known H II regions from the *Wide-field Infrared Survey Explorer* (*WISE*) Catalog of Galactic H II Regions (Anderson et al. 2014). These regions were followed up by RRL and radio continuum observations to confirm that the mid-infrared warm dust emission is associated with ionized gas (Bania et al. 2010; Anderson et al. 2011; Wenger et al. 2019). In Table 2, we list the nearest *WISE* H II region to each LOS in our sample, the distance between the center of the observations' beam and that of the nearest H II region, and the radius of the nearest H II region. The radius of a *WISE* H II region is defined by that of a circular aperture that encloses its associated mid-infrared emission. In Figure 2, we show the location of the RRL and [N II] beam and also of nearby sources in the *WISE* H II region catalog overlaid in *Spitzer* 24 μm MIPS, GLIMPSE 8 μm, and GLIMPSE 3.6 μm images tracing dust continuum emission. We also include contour lines showing the distribution of radio continuum emission around these sources. We find that most of our LOSs are located in the vicinity of H II regions but do not overlap with their brightest parts, and thus they are unlikely to be associated with compact H II regions. However, there are two exceptions, G345.7+0.0

Table 2
Nearest Known H II Region to Sample LOSs

LOS	*WISE* H II Source	Distance (arcsec)	*WISE* H II Radius (arcsec)
G305.1+0.0	G305.201+00.009	343.6	27.6
G316.6+0.0	G316.548–00.003	173.1	134.5
G337.0+0.0	G336.969–00.013	61.7	17.3
G345.7+0.0	G345.651+00.015	55.5	98.2
G342.2+0.0	G342.120+00.001	194.5	295.2
G349.1+0.0	G349.126+00.010	40.7	98.9
G000.0+0.0	G000.008+00.036	134.9	25.0
G013.9+0.0	G013.899–00.014	69.3	60.0
G030.0+0.0	G030.014+00.017	80.5	23.7
G031.3+0.0	G031.264+00.031	123.4	71.0
G049.1+0.0	G049.163–00.066	243.0	203.6

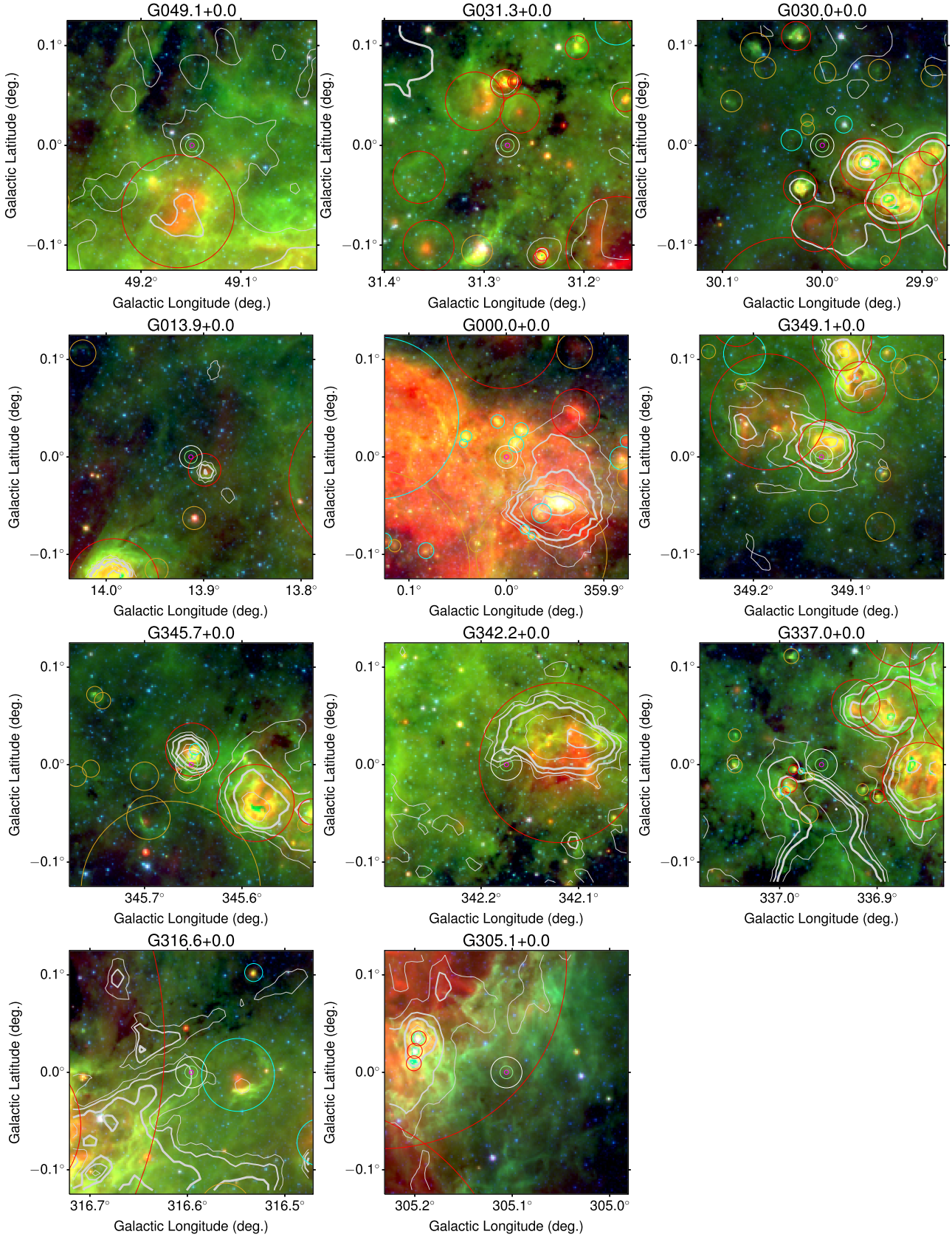

Figure 2. Location of our LOS sample overlaid with *Spitzer* 24 μm MIPS in red, GLIMPSE 8 μm in green, and GLIMPSE 3.6 μm in blue. At the center of these images, the white circle corresponds to the beam of the DSS-43 or GBT RRL observations, the magenta circle corresponds to that of the *Herschel*/HIFI [N II] 205 μm observations, and the green circle denotes approximately the size of the *Herschel*/PACS 122 and 205 μm footprint. Contours are SUMSS 843 MHz for LOSs with $305.^{\circ}1 \leqslant l \leqslant 0°$, NVSS 1.4 GHz for G013.9+0.0, and VGPS 1.4 GHz for sources with $30.^{\circ}0 \leqslant l \leqslant 49.^{\circ}1$, set to 5%, 10%, 20%, 40%, and 80% of the peak. Circles are red for known H II regions, cyan for candidates that have detected radio continuum, and orange for candidates that do not have radio continuum.

and G349.1+0.0, in which the beams of our observations partially overlap with the brightest parts of H II regions.

3. Determination of the Electron Density with [N II] and RRL Observations

3.1. [N II] 205 μm Emission

The ground electronic state of ionized nitrogen is a three fine-structure level system that results in two fine-structure transitions at 122 μm ($^3P_2$–$^3P_1$) and 205 μm ($^3P_1$–$^3P_0$). The brightness of an [N II] line integrated over frequency for an optically thin spectral line of frequency ν_{ul}, spontaneous decay rate A_{ul}, and upper-level column density N_u is given by (e.g., Goldsmith et al. 2012)

$$I = \frac{A_{ul} h \nu_{ul} N_u}{4\pi} \ [\mathrm{erg\ cm^{-2}\ s^{-1}\ sr^{-1}}], \quad (1)$$

or in terms of the main-beam temperature per unit velocity,

$$\int T_{\mathrm{mb}} dv = \frac{c^3}{2k_{\mathrm{b}}\nu_{ul}^3} I = \frac{A_{ul} h c^3 N_u}{8\pi k_b \nu_{ul}^2} [\mathrm{K\ km\ s^{-1}}]. \quad (2)$$

For the [N II] 205 μm line, we can write the column density at the upper level ($^3P_1$) in terms of the total N^+ column density as $N(^3\mathrm{P_1}) = f(^3\mathrm{P_1}) N(\mathrm{N^+})$, where $f(^3\mathrm{P_1})$ is the fractional population of the $^3\mathrm{P_1}$ level. We can therefore write Equation (2) as

$$\int T_{\mathrm{mb}}^{[\mathrm{N\ II}]} dv = \frac{A_{10} h c^3}{8\pi k \nu_{10}^2} f(^3\mathrm{P_1}) N(\mathrm{N^+}) = 5.01 \times 10^{-16} f(^3\mathrm{P_1}) N(\mathrm{N^+}) [\mathrm{K\ km\ s^{-1}}]. \quad (3)$$

For this transition, the spontaneous decay rate (Einstein's A coefficient) is $A_{10} = 2.08 \times 10^{-6}$ s^{-1}, and the rest frequency is $\nu_{10} = 1.461 \times 10^{12}$ Hz. Goldsmith et al. (2015) calculated the fractional population of the $^3\mathrm{P_1}$ and $^3\mathrm{P_1}$ levels as a function of the electron density of ionized gas, as shown in the top panel of Figure 3.

3.2. Hydrogen Recombination Line Emission

In local thermodynamical equilibrium (LTE), the main-beam temperature (in units of K) per unit velocity (km s^{-1}) of a hydrogen recombination line is given by (Rohlfs & Wilson 2004)

$$\int T^{\mathrm{RRL}} dv = 5.76 \times 10^{11} T_{\mathrm{e}}^{-3/2} \mathrm{EM} \nu^{-1}, \quad (4)$$

where the line frequency ν is in Hz, the electron temperature T_e is in K, and the EM is in cm^{-6} pc. The EM is defined as the integral of the electron volume density squared along the LOS,

$$\mathrm{EM} = \int n_e^2 dl. \quad (5)$$

The narrow range of [N II] and RRL emission as a function of velocity seen in our data set (Figure 1) indicates that it arises from discrete sources rather than from the extended diffuse WIM, which would show emission over a much wider range of velocities. Thus, we can assume that the electron density, n_e, is approximately constant along the LOS, so that this equation can be simplified to

$$\mathrm{EM} = n_e N_e \simeq n_e N(\mathrm{H^+}), \quad (6)$$

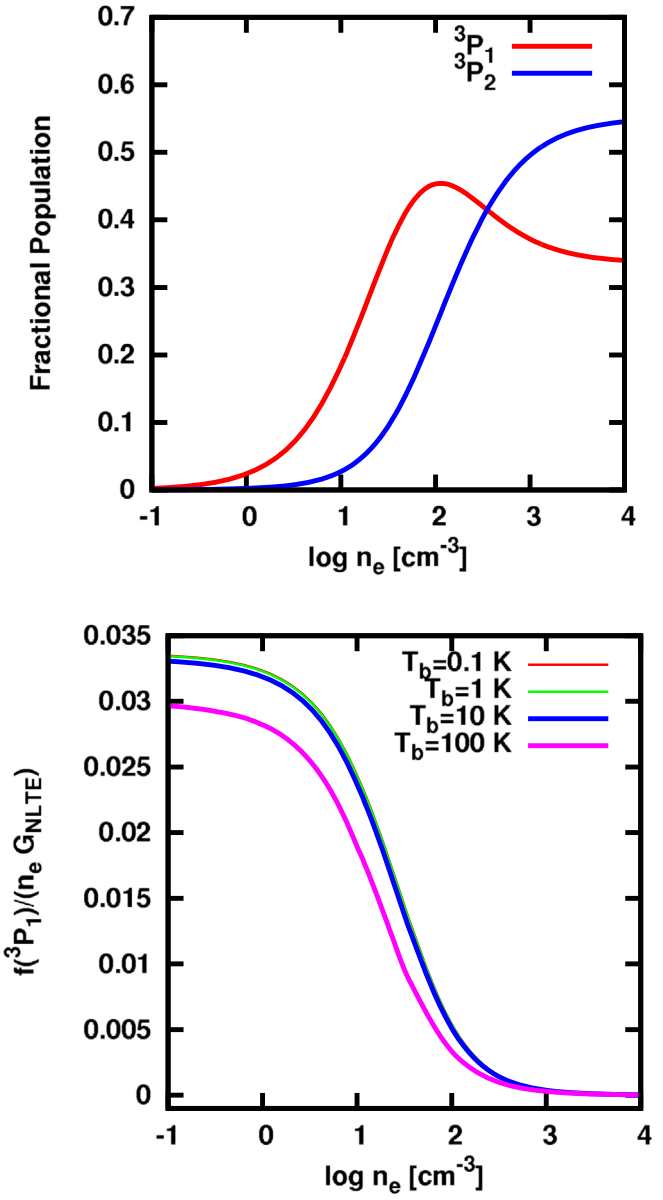

Figure 3. Top panel: fractional population in the $^3\mathrm{P_1}$ and $^3\mathrm{P_2}$ levels of ionized nitrogen as a function of the electron density for $T_e = 8000$ K. Bottom panel: dependence of the [N II] 205 μm/RRL ratio on electron density for a set of continuum brightness temperatures (see Equation (9)).

where N_e and $N(\mathrm{H^+})$ are the column densities of electrons and ionized hydrogen, respectively. We can thus write Equation (4) in terms of the $\mathrm{H^+}$ column density and electron density as

$$\int T^{\mathrm{RRL}} dv = 1.87 \times 10^{-7} \nu_{\mathrm{RRL}}^{-1} T_{\mathrm{e}}^{-3/2} n_{\mathrm{e}} N(\mathrm{H^+}), \quad (7)$$

where n_{e} is in units of cm^{-3} and $N(\mathrm{H^+})$ in units of cm^{-2}.

The hydrogen recombination line emission can be affected by deviations from local thermodynamical equilibrium. This deviation can be defined in terms of the ratio

$$G_{\mathrm{NLTE}}(n_e, T_c) = \frac{T^{\mathrm{RRL}}}{T_{\mathrm{NLTE}}^{\mathrm{RRL}}} = b_n \left[1 - \frac{1}{2}\tau_{\mathrm{c}} \beta_n\right], \quad (8)$$

where b_n and β_n are the departure coefficient and amplification factor, for a principal quantum number n, respectively, and T_c

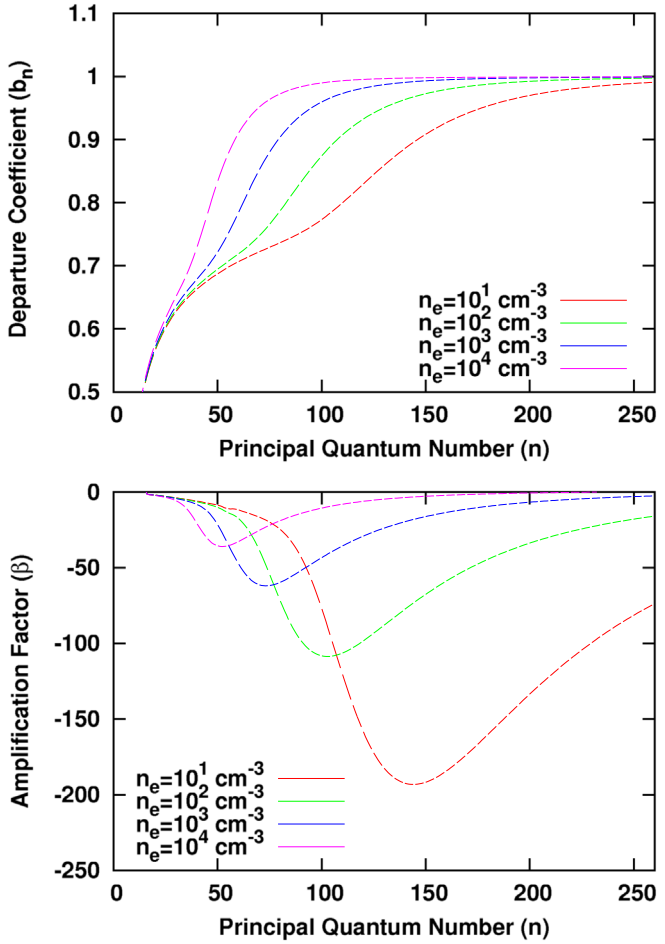

Figure 4. Effects of deviations from local thermodynamical equilibrium are well understood (Gordon & Sorochenko 2002), and a correction for these effects can be readily applied. Here we show the dependence of the departure coefficient (top panel) and amplification factor (bottom panel) as a function of principal quantum number for a range of electron densities.

and τ_c are the continuum brightness temperature and opacity, respectively, at $\nu_{\rm RRL}$. In Figure 4 we show the departure coefficient and amplification factor as a function of the principal quantum number for a set of electron densities. The continuum opacity can be derived from observations of T_c, and assuming an electron temperature, using $\tau_c = T_c/T_{\rm e}$. The effects of deviations from local thermodynamical equilibrium are well understood (Gordon & Sorochenko 2002), and a correction for these effects can be readily applied. We roughly estimated $T_{\rm c}$ in our sources by interpolating or extrapolating the flux at the frequency of our RRL observations using data at two other frequencies, assuming a power-law spectral energy distribution. For sources with $l < 0^\circ$ we used the Parkes 6 cm (5 GHz; Haynes et al. 1978) and SGPS 21 cm (1.4 GHz; Haverkorn et al. 2006) radio continuum, while for sources with $l > 0^\circ$ we used the Parkes 6 cm (5 GHz) and Nobeyama 3 cm (10 GHz; Handa et al. 1987) surveys. One exception was G049.1+0.0, where we used the Effelsberg 11 cm (2.7 Ghz; Reich et al. 1984) radio continuum map instead of the Parkes 6 cm data, as this LOS is not available in the latter survey. All maps were convolved to a common resolution of 4′. For the Galactic center position, G000.0+0.0, we extracted the brightness temperature using the GBT X-band radio continuum map presented by Law et al. (2008). The resulting continuum temperatures are listed in Table 3. We find that, except for G000.0+0.0 with $T_c = 7$ K, all continuum temperatures in our sample are below 1 K. As shown in the bottom panel of Figure 3, the [N II]-to-RRL ratio, defined below, has a weak dependence on the continuum brightness temperature, mainly influencing the low-density regime for $T_c > 10$ K. Thus, we expect that deviations from local thermodynamic equilibrium have a negligible impact in our derived electron densities. Even if the uncertainties in our derived continuum temperatures are a factor of 10, they would result in only a 3% difference in the derived electron densities.

By combining Equations (3), (7), and (8), we find that the ratio of the [N II] to RRL lines, $R_{\rm RRL}^{\rm [N\,II]}$, is a function of the electron density, the electron temperature, the continuum brightness temperature, and the relative abundance of ionized nitrogen with respect to ionized hydrogen, $X_{\rm N} = \frac{N({\rm N}^+)}{N({\rm H}^+)}$, and is given by

$$R_{\rm RRL}^{\rm [N\,II]} = 2.68 \times 10^{-9} \nu_{\rm RRL} T_{\rm e}^{3/2} \frac{f(^3{\rm P}_1)}{n_e} G_{\rm NLTE}^{-1}(n_e, T_c) X_{\rm N}. \quad (9)$$

In the bottom panel of Figure 3 we show the portion of Equation (9) that directly depends on the electron density, $f(^3{\rm P}_1)/(n_e G_{\rm NLTE}(n_e, T_c))$, as a function of electron density for several continuum brightness temperatures. The [N II]/RRL line ratio is a sensitive probe of electron density between 3 and 300 cm^{-3}, which is a typical density range for evolved H II regions in the Galactic plane (Goldsmith et al. 2015). For each of the velocity components studied here, we assume an electron temperature (in units of K) from the fit by Balser et al. (2015) as a function of galactocentric distance (in kpc),

$$T_e = (4446 \pm 301) + (467 \pm 34) R_{\rm gal}. \quad (10)$$

We also assume a nitrogen abundance relative to hydrogen, $X_{\rm N}$, from the fit as a function of galactocentric distance (in kpc) presented by Esteban & García-Rojas (2018),

$$12 + \log({\rm N/H}) = 8.21(\pm 0.09) - 0.059(\pm 0.009) R_{\rm gal}. \quad (11)$$

The distance to the Galactic center $R_{\rm gal}$ for a given velocity component with Galactic longitude l, latitude b, and local standard of rest (LSR) velocity $V_{\rm LSR}$ is given by

$$R_{\rm gal} = R_\odot \sin(l)\cos(b) \left(\frac{V(R_{\rm gal})}{V_{\rm LSR} + V_\odot \sin(l)\cos(b)} \right), \quad (12)$$

where $R_\odot$ is the distance from the Sun to the Galactic center, $V_\odot$ is the orbital velocity of the Sun with respect to the Galactic center, and $V(R_{\rm gal})$ is the rotation curve. We determined $R_{\rm gal}$ for a given l, b, and $V_{\rm LSR}$ using Equation (12) assuming the "universal" rotation curve presented by Persic et al. (1996) (see Equation (3) in Wenger et al. 2018) with parameters fitted using trigonometric parallaxes and proper motions for masers associated with massive star formation presented by Reid et al. (2014). This fit results in values of $R_\odot = 8.31$ kpc and $V_\odot = 241$ km s^{-1}. We assumed $R_{\rm gal} = 0$ kpc for the velocity components observed toward the Galactic center, as they coincide with the velocity components observed in different molecules by Henshaw et al. (2016), and that they are all interpreted to be part of the central molecular zone. In Table 3, we list the derived $R_{\rm gal}$, $T_{\rm e}$, and X_N for each velocity component.

Table 3
Derived Electron Volume Densities from the [N II] 205 μm/RRL Intensity Ratio

LOS	l (deg)	b (deg)	V_{LSR} (km s^{-1})	n_e (cm^{-3})	$N(N^+)$ (10^{16}cm^{-2})	$N(H^+)$ (10^{20}cm^{-2})	10^4[N/H][a]	10^4[N/H][b]	T_e (K)	R_{gal} (kpc)	T_C (K)
G305.1+0.0	305.106	0.0	−33.2	12.7 ± 9.6	30.7 ± 16.6	37.9 ± 32.3	0.77 ± 0.06	0.6 ± 0.1	7765 ± 386	7.1	0.3
G316.6+0.0	316.596	0.0	−48.1	8.7 ± 8.6	15.4 ± 3.6	11.3 ± 5.9	0.62 ± 0.07	0.7 ± 0.2	7439 ± 371	6.4	0.2
G316.6+0.0	316.596	0.0	−6.4	14.1 ± 12.0	7.8 ± 0.7	6.9 ± 2.5	0.62 ± 0.07	0.5 ± 0.1	8183 ± 406	8.0	0.2
G342.2+0.0	342.174	0.0	−131.2	14.0 ± 8.2	15.4 ± 3.6	11.3 ± 5.9	1.98 ± 0.41	1.2 ± 0.2	5504 ± 311	2.3	0.1
G337.0+0.0	336.957	0.0	−121.5	28.0 ± 10.3	2.4 ± 0.4	1.5 ± 0.9	0.74 ± 0.09	1.1 ± 0.2	5911 ± 318	3.1	0.4
G337.0+0.0	336.957	0.0	−76.6	41.2 ± 15.0	6.9 ± 0.4	20.0 ± 7.2	0.74 ± 0.09	0.9 ± 0.2	6473 ± 334	4.3	0.4
G345.7+0.0	345.652	0.0	−122.8	40.5 ± 18.5	9.5 ± 1.0	28.2 ± 12.4	⋯	1.3 ± 0.3	5327 ± 308	1.9	0.3
G345.7+0.0	345.652	0.0	−8.2	101.1 ± 29.6	4.9 ± 0.6	3.1 ± 1.1	⋯	0.6 ± 0.1	7859 ± 390	7.3	0.3
G349.1+0.0	349.130	0.0	17.0	62.8 ± 26.2	9.5 ± 1.0	28.2 ± 12.4	0.25 ± 0.12	0.3 ± 0.1	10600 ± 540	13.2	0.3
G349.1+0.0	349.130	0.0	−91.1	42.0 ± 13.0	4.9 ± 0.6	3.1 ± 1.1	1.16 ± 0.62	1.2 ± 0.2	5354 ± 308	1.9	0.3
G000.0+0.0	0.000	0.0	−60.5	46.5 ± 12.6	13.1 ± 1.0	8.0 ± 2.4	3.13 ± 0.24	1.6 ± 0.3	4446 ± 301	0.0	7.0
G000.0+0.0	0.000	0.0	−37.1	14.6 ± 7.2	28.2 ± 8.4	16.0 ± 9.1	3.13 ± 0.24	1.6 ± 0.3	4446 ± 301	0.0	7.0
G000.0+0.0	0.000	0.0	12.8	39.7 ± 14.2	5.4 ± 1.1	3.3 ± 1.4	3.13 ± 0.24	1.6 ± 0.3	4446 ± 301	0.0	7.0
G000.0+0.0	0.000	0.0	95.0	11.3 ± 6.5	10.6 ± 4.1	6.0 ± 4.0	3.13 ± 0.24	1.6 ± 0.3	4446 ± 301	0.0	7.0
G013.9+0.0	13.913	0.0	45.5	28.6 ± 12.3	1.3 ± 0.3	1.1 ± 0.7	1.80 ± 0.51	0.9 ± 0.2	6511 ± 336	4.4	0.4
G013.9+0.0	13.913	0.0	30.3	166.3 ± 44.2	0.7 ± 0.1	0.8 ± 0.2	1.80 ± 0.51	0.8 ± 0.2	6944 ± 351	5.3	0.4
G030.0+0.0	30.000	0.0	95.4	17.6 ± 9.9	6.3 ± 2.2	5.4 ± 3.6	1.91 ± 0.35	0.9 ± 0.2	6502 ± 336	4.4	0.6
G031.3+0.0	31.277	0.0	100.4	7.9 ± 7.9	31.9 ± 29.8	26.6 ± 31.3	1.04 ± 0.13	0.9 ± 0.2	6488 ± 336	4.4	0.4
G031.3+0.0	31.277	0.0	38.0	108.8 ± 46.6	1.6 ± 0.1	1.9 ± 0.7	1.04 ± 0.13	0.7 ± 0.2	7407 ± 369	6.3	0.4
G049.1+0.0	49.149	0.0	59.7	10.4 ± 9.2	3.8 ± 2.6	4.2 ± 4.1	1.03 ± 0.25	0.7 ± 0.2	7351 ± 367	6.2	0.2

Notes.
[a] Nitrogen abundance relative to hydrogen derived by matching electron densities derived in our work with those derived from the [N II] 122 μm/205 μm ratio.
[b] Nitrogen abundance relative to hydrogen derived from the fit presented by Esteban & García-Rojas (2018).

3.3. Uncertainties

The main factors influencing the uncertainties in the derivation of electron densities from the [N II]/RRL ratio are those arising from the uncertainties in the assumed electron temperature, the assumed relative abundance of nitrogen with respect to hydrogen, and the uncertainties in the measurements. The typical scatter in the electron temperature found by Quireza et al. (2006) is about ±350 K and results in a typical 13% uncertainty in the derived electron density. The typical scatter from the fit to X_N as a function of galactocentric distance presented by Esteban & García-Rojas (2018) is about 23%, resulting in a typical 44% uncertainty in the derived electron density. We estimated the uncertainty in the [N II]/RRL ratio by propagating those of the integrated intensities of the [N II] and RRL lines. We find typical uncertainties of 20% in the measurement of the [N II]/RRL ratio. To estimate the total error in our electron density measurements, we added the contribution from each source of uncertainty in quadrature. The total error for the derived electron density is typically 49%.

3.4. Beam-dilution Effects

In our analysis we use data at different angular resolutions (16″ for [N II] and 84″ or 115″ for the RRL data), and therefore our derived electron densities can be affected by beam-dilution effects. In Appendix A, we evaluated the effects of beam dilution in our sample using different methods. We applied a correction factor to the 16″ [N II] data using spatial information provided by *Herschel*/PACS observations from 16″ (single pixel) to 47″ (5 × 5 pixel average). We also corrected the RRL data for beam-dilution effects between 47″, 84″, and 115″, using the spatial information provided by high-resolution radio continuum data. We summarize the dilution factors, and their impact on the derived electron densities, in Table 5. By using these dilution factors, we find that the derived electron densities would vary by ∼15% for sources observed in RRLs at 84″ and by ∼36% for sources observed at 115″. We also applied beam-dilution corrections to the data in the G000.0+0.0 and G345.7+0.0 LOSs derived by comparing RRL data observed at different angular resolutions. By applying these dilution factors to our data, we are estimating electron densities on scales of 47″, except for G000.0+0.0, where densities are derived on scales of 16″.

4. Discussion

4.1. Volume Densities

Using the method described in Section 3, we derived electron densities for 21 velocity components in the 11 LOSs analyzed here. To determine the [N II]/RRL ratio for each velocity component in the observed LOSs, we decomposed the [N II] and RRL emission into a set of Gaussian components (Table 6), which are later combined to determine this line ratio. We then use Equation (9) to solve for the electron density for each velocity component, with an assumed electron temperature and nitrogen abundance relative to hydrogen, as discussed above. There are cases when the data are not easily decomposed into Gaussian components owing to blended components, in particular for the RRL emission, as their line widths are significantly larger than those for [N II]. In this case we used the intensity integrated over a velocity range that encompasses the velocity component for the derivation of the [N II]/RRL ratio.

In Table 3, we list the derived electron density, LSR velocity, assumed electron temperature, nitrogen fractional abundance, N^+ and H^+ column densities, continuum temperature, and galactocentric distance for each velocity component analyzed here. We find that the electron densities in our sample range between 8 and 170 cm^{-3} with an average value of 41 cm^{-3}.

In Figure 5, we illustrate our electron density determination by showing the observed RRL emission together with that predicted from the corresponding [N II] emission and a set of electron densities (color-coded; see Equation (9)). Electron density solutions correspond to those where the observed RRL and its predicted emission coincide. Note that owing to their different masses, the thermal line widths of H^+ are expected to be significantly larger[7] than those of N^+. To enable the comparison shown in Figure 5, we convolved the [N II] lines with a Gaussian function with an FWHM that results in an [N II] profile that matches the thermal line width for H^+.

4.2. Comparison with Densities Derived Using 122 μm/250 μm Ratio

Goldsmith et al. (2015) used low spectral resolution *Herschel*/PACS observations of the [N II] 122 and 205 μm lines to derive a characteristic electron density along the LOSs across the Galactic plane, including the 11 LOSs studied here. The ratio of [N II] 122 μm to 205 μm provides an accurate determination of the electron density that does not depend on nitrogen abundance and has a weak dependence on electron temperature. A comparison with our velocity-resolved determination of the electron density provides an opportunity to understand how this characteristic density determined by *Herschel*/PACS relates to the actual volume density distribution along the LOS and also allows us to test our approach to determine the electron density.

For the low-density regime, the electron density derived from the integrated ratio of [N II] 122 μm to 205 μm is the nitrogen column density weighted average of all components along the LOS. However, for the density regime found in our LOSs the electron density has a less straightforward interpretation.

The [N II] 122 μm/205 μm ratio for an LOS with n velocity components with integrated intensities $I^i_{122\,\mu\mathrm{m}}$ and $I^j_{205\,\mu\mathrm{m}}$ is given by

$$\frac{I_{122\,\mu\mathrm{m}}}{I_{205\,\mu\mathrm{m}}} = \frac{\sum_i^n I^i_{122\,\mu\mathrm{m}}}{\sum_j^n I^j_{205\,\mu\mathrm{m}}}. \quad (13)$$

Substituting Equation (1) in the numerator of Equation (13) and considering that the upper-level column density, N_u, is equal to the ionized nitrogen column density times the fractional abundance of the upper level, $N(N^+)f_2(n_e)$, results in

$$\frac{I_{122\,\mu\mathrm{m}}}{I_{205\,\mu\mathrm{m}}} = \frac{A_{21}h\nu_{122\mu\mathrm{m}}}{4\pi}\frac{\sum_i^n N^i(N^+)f_2^i(n_e^i)}{\sum_j^n I^j_{205\,\mu\mathrm{m}}}. \quad (14)$$

Also using Equation (1), we can express the ionized nitrogen column density as a function of the [N II] 205 μm line intensity (for which we have information about its velocity distribution) as

$$N(N^+) = \frac{4\pi I_{205\,\mu\mathrm{m}}}{A_{10}h\nu_{205\,\mu\mathrm{m}}f_1(n_e)}. \quad (15)$$

Substituting this expression in Equation (14) allows us to write the [N II] 122 μm/205 μm ratio as a function of the [N II] 205 μm intensity and the $f_1(n_e)$ and $f_2(n_e)$ upper-level fractions as

$$\frac{I_{122\,\mu\mathrm{m}}}{I_{205\,\mu\mathrm{m}}} = \frac{A_{21}\nu_{122\mu\mathrm{m}}}{A_{10}\nu_{205\,\mu\mathrm{m}}}\frac{\sum_i^n I^i_{205\,\mu\mathrm{m}}\frac{f_2^i(n_e^i)}{f_1^i(n_e^i)}}{\sum_j^n I^j_{205\,\mu\mathrm{m}}}, \quad (16)$$

and thus it can be evaluated given the electron densities derived from the [N II]/RRL ratio and the observed integrated intensities of the [N II] 205 μm line in each velocity component along a given LOS. This estimated ratio can be used to evaluate the characteristic electron density using Equation (21) in Goldsmith et al. (2015). Note that the electron densities published by Goldsmith et al. (2015) are those for the [N II] 122 μm to 205 μm intensities averaged over the 47″ footprint of the *Herschel*/PACS instrument. In our calculations we use instead, to avoid uncertainties due to beam dilution, the *Herschel*/HIFI spectra at a resolution of 16″ and the [N II] 122 μm intensities averaged from the *Herschel*/PACS footprint with a Gaussian-weighted function with an FWHM of 16″. These different approaches result in slightly different electron densities.

In Table 4, we compare the characteristic electron density derived from Equation (16) with that resulting from the observed [N II] 122 μm/205 μm ratio by *Herschel*/PACS. In Figure 6, we compare the LOS-averaged electron density with those derived using the 122 μm/205 μm lines by Goldsmith et al. (2015). While there is general agreement between these two methods, the scatter can arise from the assumed nitrogen fractional abundance in our calculations.

4.3. Nitrogen Abundances Relative to Hydrogen

The distribution of element abundances in the disk of galaxies is a fundamental observational constraint for models of the formation and evolution of the Milky Way. Nitrogen is formed in "primary" and "secondary" processes in massive and intermediate-mass stars (Johnson 2019), and thus its abundance distribution is related to the star formation history as a function of galactocentric distance in the Milky Way. Observations of optical lines of [N II] in nearby H II regions, where dust extinction obscures these lines moderately, have been used to infer that the abundance of nitrogen increases with galactocentric distance from the outer Galaxy up to $R_{\mathrm{gal}} = 6$ kpc (Esteban & García-Rojas 2018). Due to increased dust extinction, optical studies are, however, unable to probe the inner Galaxy, where stellar processing was enhanced in the past. The far-infrared lines of [N II] have the advantage of being unobscured and thus allow us to determine element abundances over larger distances, including the inner Galaxy, where most of the star formation takes place (Simpson et al. 1995, 2004). In the following, we use our observations of RRLs together with those of the [N II] 205 and 122 μm lines to derive nitrogen abundances in our sample, allowing us to sample the inner Galaxy.

The [N II] 122 μm/205 μm ratio provides an accurate determination of the electron density that is independent of nitrogen abundance and has a weak dependence of electron temperature. By matching electron temperatures derived from the [N II] 205 μm/RRL ratio to those derived from the [N II] 122 μm/205 μm ratio, we can therefore determine the abundance of ionized nitrogen relative to ionized hydrogen in our sample.

[7] For example, for $T_e = 8000$ K the thermal line width of a hydrogen RRL line is 19 km s^{-1}, while for the [N II] line it is 5 km s^{-1}. Note that pressure broadening is not expected to be significant in the density regime that we are sampling (Brocklehurst & Seaton 1972).

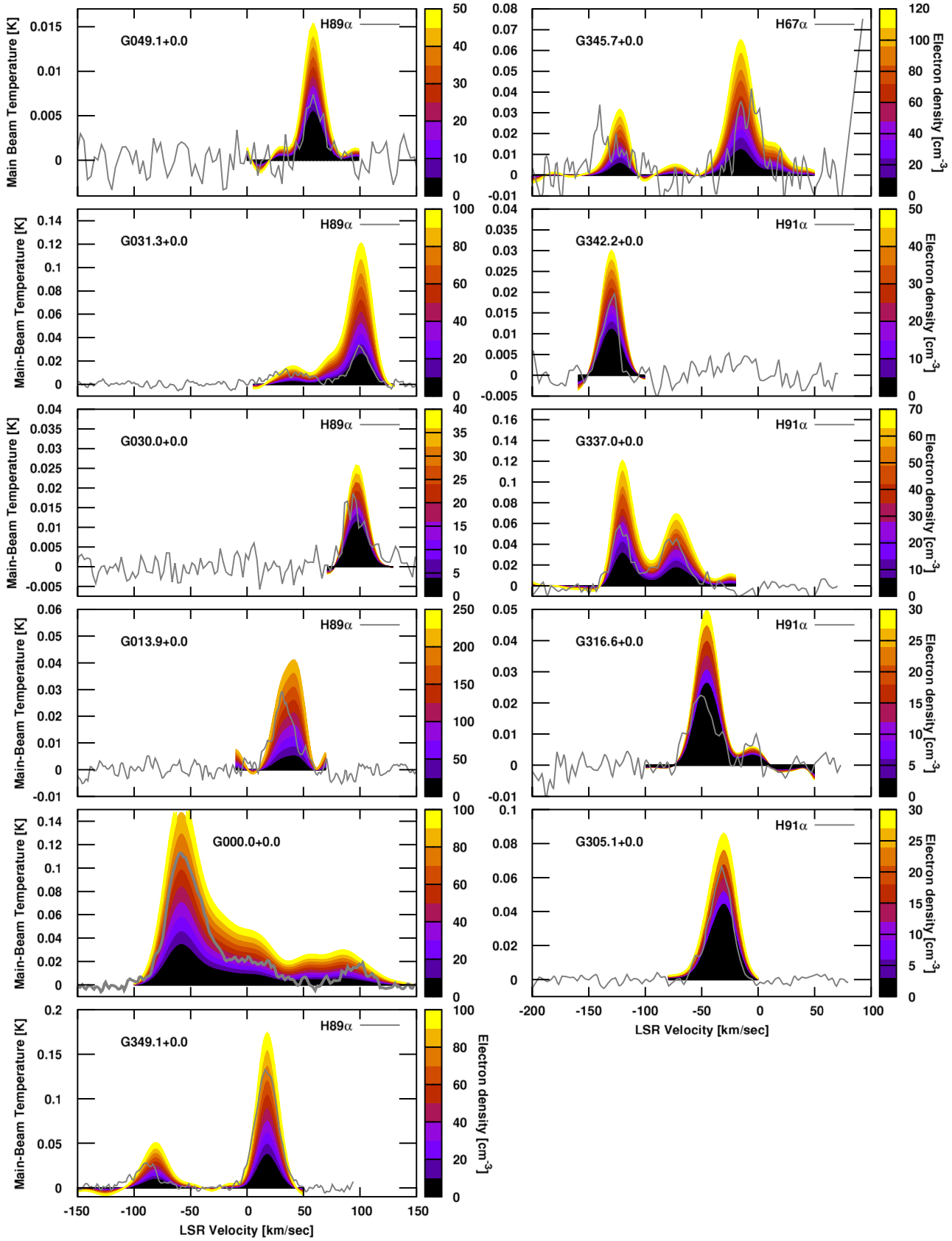

Figure 5. Electron density solutions for our sample sight lines. The gray lines show observed RRL emission. The color-coded lines are the predicted RRL emission for the observed [N II] spectra and a given electron density (see Section 4.1), with the corresponding volume densities shown in the color wedge on the right axis. Electron density solutions correspond to those where the observed RRL and its predicted emission coincide.

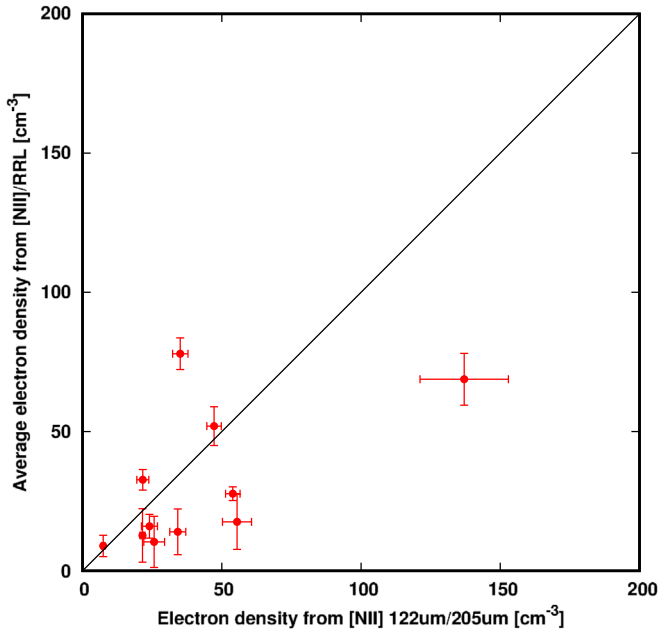

Figure 6. Electron density derived from the [N II] 205 μm/RRL ratio as a function of that derived from the [N II] 122 μm/205 μm ratio presented by Goldsmith et al. (2015). The black straight line represents an $n_e^{[\mathrm{N\,II}]} = n_e^{\mathrm{RRL}}$ relationship.

The ionized nitrogen abundance, X_{N^+}, can be written in terms of the ionized nitrogen column density, $N(\mathrm{N}^+)$, and the EM, derived from the RRL observations (Equations (5) and 6) as

$$X_{\mathrm{N}^+} = \frac{N(\mathrm{N}^+)}{N(\mathrm{H}^+)} = \frac{n_e N(\mathrm{N}^+)}{\mathrm{EM}}, \quad (17)$$

which in turn can be written in terms of the [N II] 205 μm line intensity using Equation (15) as

$$X_{\mathrm{N}^+} = \frac{4\pi n_e I_{205\,\mu\mathrm{m}}}{A_{10} h\nu_{205\,\mu\mathrm{m}} f_1(n_e)\mathrm{EM} G_{\mathrm{NLTE}}^{-1}(n_e, T_e)}. \quad (18)$$

Using this equation, we determined the ionized nitrogen abundance in LOSs with a single velocity component (three in our sample) by using the observed $I_{205\,\mu\mathrm{m}}$ and EM and assuming an electron density that results from the [N II] 122 μm/205 μm ratio observed with *Herschel*/PACS.

For spectra with two velocity components we find that there is typically a large number of combinations of the electron density of each component that results in the same observed [N II] 122 μm/205 μm ratio (see Equation (16)), and thus the X_{N^+} of each individual component cannot be uniquely determined. However, the velocities of the components in most of these LOSs (5 out of 7) are similar to each other and have distances to the Galactic center that are within 2 kpc from each other. Assuming that X_{N^+} varies only over large scales, we can therefore use a constant value of X_{N^+} for sources within <2 kpc scales. In this case, the electron density, n_e^i, of any component is related to that, n_e^j, of any other component by

$$\frac{n_e^i I_{205\,\mu\mathrm{m}}^i}{f_1(n_e^i) EM^i G_{\mathrm{NLTE}}^{-1}(n_e^i, T_e^i)} = \frac{n_e^j I_{205\,\mu\mathrm{m}}^j}{f_1(n_e^j) EM^j G_{\mathrm{NLTE}}^{-1}(n_e^j, T_e^j)}, \quad (19)$$

and this expression can be used in combination with Equation (16) to solve for the electron densities for all velocity components. This information can then be used to determine X_{N^+} for the LOS using Equation (18).

Table 4
LOS-averaged Volume Densities

LOS	$n_e\left(\frac{[\mathrm{N\,II}]205\,\mu\mathrm{m}}{\mathrm{RRL}}\right)$ (cm^{-3})	$n_e\left(\frac{[\mathrm{N\,II}]122\,\mu\mathrm{m}}{[\mathrm{N\,II}]205\,\mu\mathrm{m}}\right)$ (cm^{-3})
G305.1+0.0	12.7 ± 9.6	21.5 ± 0.9
G316.6+0.0	8.9 ± 3.8	7.4 ± 0.6
G337.0+0.0	32.7 ± 3.7	21.6 ± 2.2
G342.2+0.0	14.0 ± 8.2	34.2 ± 2.9
G345.7+0.0	77.9 ± 5.7	35.1 ± 2.8
G349.1+0.0	52.0 ± 7.0	47.2 ± 2.6
G000.0+0.0	27.7 ± 2.5	54.0 ± 2.6
G013.9+0.0	68.8 ± 9.3	137.1 ± 15.9
G030.0+0.0	17.6 ± 9.9	55.5 ± 5.2
G031.3+0.0	16.0 ± 4.3	24.0 ± 2.9
G049.1+0.0	10.4 ± 9.2	25.7 ± 3.7

There are two LOSs in our sample, G345.7+0.0 and G349.1+0.0, for which we cannot assume a constant, X_{N^+}, as their velocity components are well separated, corresponding to galactocentric distances that differ by more than 5 kpc. In the case of G349.1+0.0 the electron density solutions obtained using the [N II] 205 μm/RRL also satisfy Equation (16) within their uncertainties, and we therefore assume a solution for the electron densities that is the closest electron density combination that can satisfy both the observed [N II] 205 μm/RRL and [N II] 122 μm/205 μm ratios. This similarity between solutions is not the case for G345.7+0.0, and therefore we excluded these LOSs from our estimate of X_{N^+}.

In Figure 7 we present the derived ionized nitrogen fractional abundances as a function of galactocentric distance. We also include a straight solid line corresponding to the fit by Esteban & García-Rojas (2018), which is determined for a range of 6–16 kpc in galactocentric distance. We also include the extrapolation of this relationship to $R_{\mathrm{gal}} = 0$ kpc as a dashed line. Our determination of X_{N^+} corresponds mostly to the range $R_{\mathrm{gal}} < 6$ kpc, which is not accessible for optical studies such as that from Esteban & García-Rojas (2018). We fitted a straight line to all data in Figure 7 using the orthogonal bi-variate error and intrinsic scatter method (BES;[8] Akritas & Bershady 1996), including a bootstrap resampling error analysis, resulting in

$$12 + \log(\mathrm{N}^+/\mathrm{H}^+) = 8.40(\pm 0.21) - 0.076(\pm 0.034) R_{\mathrm{gal}}. \quad (20)$$

We checked whether this fit was influenced by the single data point at 13.2 kpc, by refitting the data with all data but excluding this data point. We found no significant difference between the resulting fit and that found for the entire data set. We find that our derived ionized nitrogen abundances have a slope that is consistent with that found by Esteban & García-Rojas (2018) in the outer Galaxy. A flattening in the abundance distribution of different species in the inner Galaxy has been inferred by observations of Cepheids and red giants (Hayden et al. 2014; Martin et al. 2015; Andrievsky et al. 2016), suggesting different star formation histories between the inner and outer Galaxy, with the star formation rate in the inner Galaxy possibly being reduced by dynamical effects such as

[8] http://www.astro.wisc.edu/~mab/archive/stats/stats.html

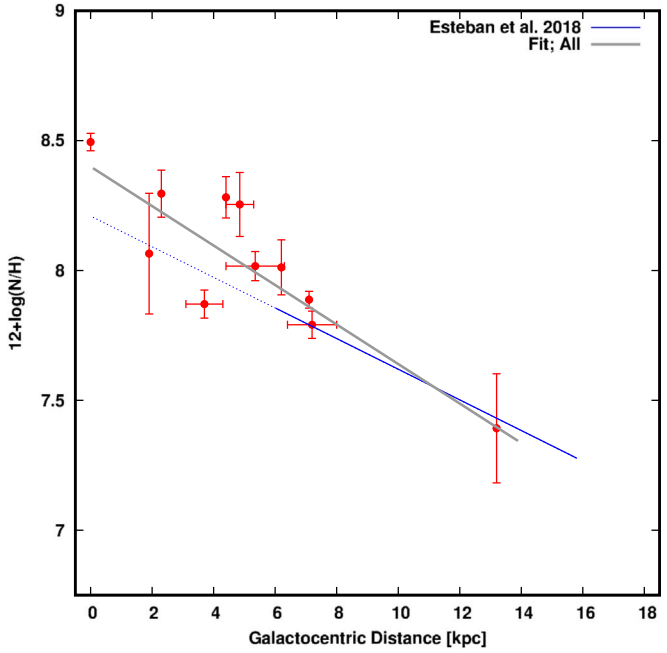

Figure 7. Nitrogen abundance relative to hydrogen as a function of galactocentric distance. The blue straight line represents the fit to optical data from Esteban & García-Rojas (2018), and an extrapolation of this relationship to $R_{\rm gal} = 0$ kpc is shown as a blue dashed line. The fit to our data is shown as a gray line.

the Galactic bar. While the distribution of nitrogen abundances in our data is not consistent with the suggested flattening in the inner Galaxy, it cannot be discarded with our data owing to the uncertainties in the fit, which in turn result from the small number of samples. As mentioned above, we are currently conducting a survey of all GOT C+ LOSs observed in [N II] by Goldsmith et al. (2015), with the GBT and DSS-43 telescopes, which will allow us to increase significantly our sample in the inner Galaxy, resulting in an accurate determination of the distribution of nitrogen abundances in the inner Galaxy.

In H II regions, nitrogen is efficiently singly ionized by charge exchanges with protons (Langer et al. 2015), collisional ionization with electrons, and an extreme ultraviolet (EUV) field. Higher ionization states of nitrogen are possible in the presence of a large EUV field in the close vicinity of massive star clusters. Higher ionization states of nitrogen need to be accounted for to obtain a determination of the total nitrogen abundance, $X_{\rm N}$, from our derived ionized nitrogen abundance. The abundance of higher ionization states of nitrogen can be estimated with observations of [N III] and [O III] lines (N^+ and O^+ have similar ionization potentials: 29.6 and 35.1 eV, respectively). But these observations are not always available. Esteban & García-Rojas (2018) observed optical collisonally excited lines of N in low-ionization H II regions, where the abundance of multiple ionized nitrogen is negligible, and thus $X_{\rm N} \simeq X_{\rm N^+}$. As mentioned in Section 3.4, except for G345.7 +0.0 and G349.1+0.0, our LOSs are not directly associated with the brightest parts of known H II regions and represent the extended envelopes of these H II regions. Additionally, the derived electron densities are lower than those typically found in compact H II regions. We can therefore assume that the ionized gas probed in our sample is also low ionization, and most of the gas-phase nitrogen is singly ionized. Note that even if multiple ionization states of nitrogen need to be accounted for, we do not expect a significant variation of this contribution to the total nitrogen abundance to vary with galactocentric distance, and thus the slope of the relationship between our derived nitrogen abundances and galactocentric distance should not vary significantly.

4.4. The Nature of the Dense WIM

The derived densities in our sample confirm those derived by Goldsmith et al. (2015) over a larger sample in the Galactic plane, but at lower spectral resolution. The observed [N II] and RRL emission arises from a plasma that is denser than the diffuse WIM ($\lesssim$0.1 cm^{-3}; Cordes & Lazio 2002; Haffner et al. 2009) but has lower densities compared to those typical of (ultra)compact H II regions ($>5 \times 10^3$ cm^{-3}; Kurtz 2005). The spectrally resolved observations allowed us to study the electron density of these media along the LOS, showing that the RRL and [N II] emission arises from discrete velocity components rather than from the extended diffuse WIM, which would show emission over a much wider range of velocities. By comparing with the *WISE* catalog of known H II regions (Table 2, Figure 2), we find that most of our LOSs are located in the vicinity of H II regions but do not overlap with their brightest parts, and thus are unlikely to be associated with compact H II regions. This dense plasma appears to be widely distributed in the Galactic plane, as suggested by similar densities detected in a larger number of LOSs by Goldsmith et al. (2015) and at the edge of the central molecular zone by Langer et al. (2015), and thus can represent a significant fraction of the ionized gas in our Galaxy. Further investigations of this widespread dense ionized gas component, by large-scale mapping of [N II] and RRL emission, are important for fully characterizing this component and to assist the interpretation of observations of ionized gas in extragalactic sources.

5. Conclusions

We presented a method to derive the electron density of ionized gas using the ratio of the [N II] 205 μm line to an RRL. We use this method to derive electron densities of 21 velocity components in 11 LOSs observed in spectrally resolved [N II] 205 μm with the *Herschel*/HIFI and SOFIA/GREAT instruments and in RRLs with the GBT and NASA Deep Space Network DSS-43 telescope. We summarize our results as follows:

1. We found typical electron densities between 6 and 170 cm^{-3}, with an average value of 41 cm^{-3}, which are consistent with those derived at low spectral resolution using the [N II] 122 μm/205 μm ratio with *Herschel*/PACS and are significantly larger than those characteristic of the diffuse WIM but lower than those expected for (ultra)compact H II regions.
2. By matching the electron densities derived from the [N II] 205 μm/RRL ratio and the [N II] 122 μm/205 μm ratio, we derive the fractional abundance N/H for most of our velocity components.
3. We studied the dependence of the N/H ratio with galactocentric distance in the inner 8 kpc of the Milky Way, which is a range that is not accessible (in particular for $R_{\rm gal} < 6$ kpc) to optical studies owing to dust extinction. We find that the distribution of nitrogen abundances in the inner Galaxy derived from our data has a slope that is consistent with that found in the outer

Galaxy in optical studies. This result is inconsistent with suggestions of a flatter distribution of the nitrogen abundance in the inner Galaxy. This trend, however, will need to be confirmed with a larger [N II] and RRL data set.

The method presented here to derive electron densities can be expanded to a much larger database using the *Herschel*/PACS [N II] 122 and 205 μm survey by Goldsmith et al. (2015), consisting of about 100 LOSs and our complete DSS-43/GBT survey of the Galactic plane. These observations will allow us to obtain a more complete sample of electron densities in the Galactic plane and to derive the N/H gradient in our Galaxy.

This research was conducted at the Jet Propulsion Laboratory, California Institute of Technology, under contract with the National Aeronautics and Space Administration. This project made use of the Smithsonian Astrophysical Observatory 4 × 32k-channel spectrometer (SAO32k) and the *TAMS observatoryCtrl* observing system, which were developed by L. Greenhill (Center for Astrophysics), I. Zaw (New York University Abu Dhabi), D. Price, and D. Shaff, with funding from SAO and the NYUAD Research Enhancement Fund and in-kind support from the Xilinx University Program. We thank West Virginia University for its financial support of GBT operations, which enabled the observations for this project. The National Radio Astronomy Observatory is a facility of the National Science Foundation operated under cooperative agreement by Associated Universities, Inc. L.D.A. and M.L. are supported by NSF grant AST1516021 to L.D.A. © 2019 California Institute of Technology. U.S. Government sponsorship acknowledged.

Facilities: GBT, SOFIA, *Herschel*.

Software: TMBIDL (Bania et al. 2014), GILDAS/CLASS (Pety 2005).

Appendix A
Beam Dilution Correction

Our analysis is carried out using data at different angular resolutions (16″ for [N II] and 84″ or 115″ for the RRL data), and therefore our derived electron densities can be affected by beam-dilution effects. As a first step to address the effects of beam dilution, we checked whether any of our LOSs are associated with known H II regions in the *WISE* catalog (Table 2 and Figure 2). We found that most of our LOSs are not directly associated with compact H II regions but are located in their vicinity. There are two LOSs in our sample (G345.7+0.0 and G349.1+0.0) in which the RRL beam partially overlaps with H II regions in the *WISE* catalog. In the following we investigate how the results of this paper are affected by beam dilution effects. We studied beam-dilution effects in the [N II] data using *Herschel*/PACS data and in the RRL data using radio continuum data. The dilution factors derived from these data sets, as well as their impact in the derived electron density in each velocity component, are summarized in Table 5.

While the *Herschel*/HIFI [N II] data have an angular resolution of 15.″7, we also have observations of the same line done with the PACS instrument, which has a 5 × 5 pixel grid, with a pixel separation of 9.″4, corresponding to a footprint of 47″ in the sky. Note, however, that the PACS data are velocity unresolved and thus provide information about the integrated intensity of the [N II] over 47″ scales. To study the beam dilution of the [N II] line over 47″ scales, we used the PACS [N II] footprint to calculate the intensity at 15.″7 and 47″ by averaging the data weighted by a two-dimensional Gaussian function with FWHM corresponding to 15.″7 and 47″, respectively. We find a typical variation of the [N II] intensity of about 15% on angular scales extending from 15.″7 to 47″. We used the derived beam-dilution factors to correct our data using the method described in Appendix A.2 in Pineda et al. (2017), with the exception of G000.0+0.0, in which we have data available at 16″ resolution, as discussed below.

We also studied beam-dilution effects over a larger range of angular resolutions, by using radio continuum observations from the THOR+VGPS (λ = 20 cm; angular resolution 25″; coverage $l = 14.^\circ5$ to $67.^\circ4$; Beuther et al. 2016), MAGPIS (20 cm; 6″ ; $l = 5^\circ$ to $48.^\circ5$; Helfand et al. 2006), and MGPS-2 (35.6 cm; 45″–57.″5; $l = 245^\circ$ to 365°; Murphy et al. 2007) surveys. The THOR+VGPS and MAGPIS maps have been corrected for missing short spacings, and the MGPS-2 data are sensitive to angular scales between 45″ and 1200″–1800″, thus encompassing the angular scales sampled by the *Herschel*/PACS, GBT, and DSS-43 observations. We used the THOR +VGPS data of our sample with $l > 14.5^\circ$, the MAGPIS data for G013.9+0.0, and the MGPS-2 data for sources with $l < 365^\circ$. Given that RRL emission is detected in our sample, we assume that radio continuum emission is dominated by thermal bremsstrahlung (free–free) emission from the ionized gas rather than from synchrotron radiation, and thus its morphology corresponds to that of the ionized gas. We convolved these maps to 47″ (except for the MGPS-2 data, for which we use its original resolution), 84″, and 115.″2 to match those of the *Herschel*/PACS, GBT, and DSS-43 data, respectively. We find that intensities vary typically by 6% when smoothing from 47″ to 84″ and by 14% when smoothing from 47″ to 115″. These variations result in typical variations in the derived electron densities of about 38%. Note that two LOSs, G337.0+0.0 and G342.2+0.0, are not detected in radio

Table 5
Beam Dilution Correction

LOS	Velocity (km s^{-1})	$I_{15.''7}/I_{47''}$	$I_{84''}/I_{47''}$	$I_{115''}/I_{47''}$	n_e^*/n_e[a]
	…	…	…	…	…
G305.1+0.0	−33.2	1.11	…	0.97	1.26
G316.6+0.0	−48.1	1.11	…	1.26	…[b]
G316.6+0.0	−6.4	1.11	…	1.26	2.03
G342.2+0.0	−131.2	1.18	…	1.00	1.61
G337.0+0.0	−121.5	1.22	…	1.00	1.54
G337.0+0.0	−76.6	1.22	…	1.00	1.31
G345.7+0.0	−122.8	1.25	…	1.00	1.35
G345.7+0.0	−8.2	1.25	…	1.00	1.10
G349.1+0.0	17.0	1.14	1.01	…	1.18
G349.1+0.0	−91.1	1.14	1.01	…	1.20
G013.9+0.0	45.5	0.99	0.89	…	0.83
G013.9+0.0	30.3	0.99	0.89	…	0.90
G030.0+0.0	95.4	1.15	0.96	…	1.28
G031.3+0.0	100.4	1.07	0.96	…	1.18
G031.3+0.0	38.0	1.07	0.96	…	1.03
G049.1+0.0	59.7	0.89	1.05	…	0.80

Notes.
[a] Ratio of the beam-dilution-corrected electron density (n_e^*) to that resulting when no beam dilution is applied (n_e).
[b] The electron density derived without a beam-dilution correction in this velocity component is undefined.

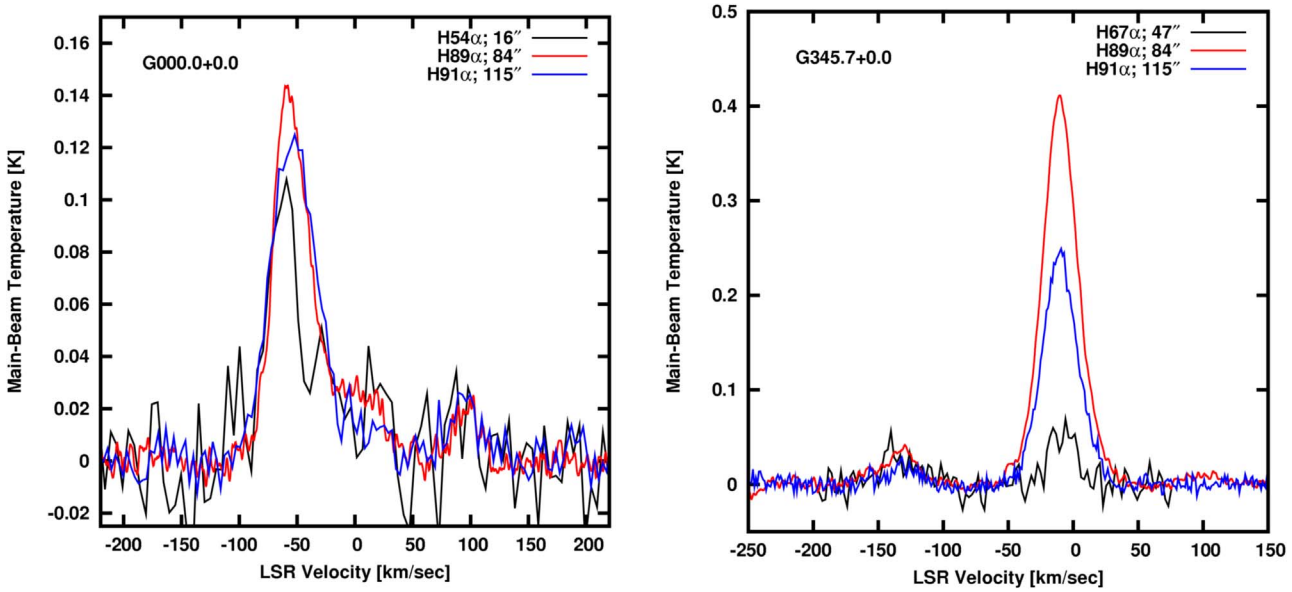

Figure 8. Left panel: G000.0+0.0 LOS observed in the H54α, H89α, and H91α, at 16″, 84″, and 115″ angular resolution, respectively. Right panel: G345.70+0.0 LOS observed in the H67α, H89α, and H91α, at 47″, 84″, and 115″ angular resolution, respectively. All RRL intensities shown here were scaled to correspond to that of the H89α line.

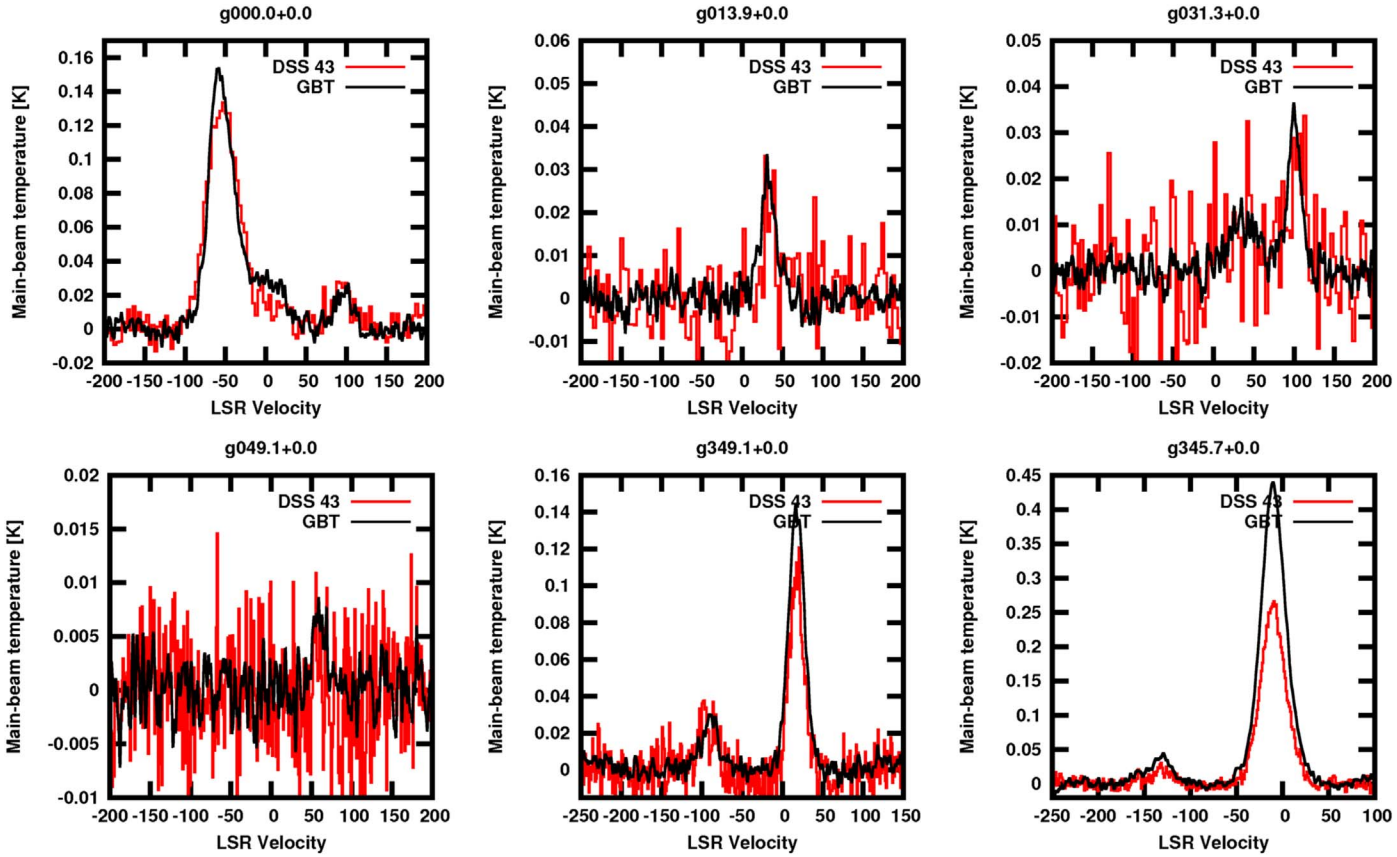

Figure 9. Comparison between hydrogen recombination line observations from the GBT and the DSS-43 telescopes. We find good agreement between these two lines, despite the different angular resolution of the observations (115″ vs. 84″).

continuum emission in the MGPS-2 survey. They both are adjacent to extended H II regions (Figure 2) that do not overlap significantly with the *Herschel*/PACS footprint and DSS-43 beam. We therefore assume that there are no significant spatial variations between 47″ and 115″ in these LOSs, and we thus use a dilution factor of unity for these sources. By applying these dilution factors to our data, we are estimating electron densities on scales of 47″.

We made a better estimate of the beam-dilution effects in two LOSs by comparing their RRL observations taken at

different angular resolutions. In the left panel of Figure 8, we show the G000.0+0.0 LOS observed in the H54α and H89α lines with the GBT at 16″ and 84″, respectively, and in the H91α line observed with the DSS-43 telescope at 115″. All RRL observations shown in Figure 8 were scaled to correspond to the intensity of the H89α line. As discussed in Section 2.2, when scaling RRLs with large differences between their principal quantum numbers, deviations from LTE, which depend on electron density and temperature (Equation (8)), need to be taken into account. We therefore considered non-LTE effects when scaling the H54α line intensities to correspond to that of the H89α line, by assuming the electron density and temperatures shown in Table 3 for G000.0+0.0. Note that the contribution from non-LTE effects to the scaling factor between H54α and H89α varies weakly with electron density in the uncertainty range in this quantity that results from beam-dilution effects and other error sources (Section 3.3). While the velocity distribution is similar at these different angular resolutions, we find that the 84″ H89α data are a factor of 1.5 times brighter than those at 16″. Given that the H89α observations have the highest signal-to-noise ratio, we will use this spectrum for our analysis, but with the factor 1/1.5 applied to account for the beam-dilution effects in our data. In the right panel of Figure 8, we show the H67α, H89α, and H91α lines, at 47″, 84″, and 115″, respectively, in the G345.7+0.0 LOSs. As above, we accounted for non-LTE effects when scaling the H67α line intensity to that of the H89α line. This LOS is associated with a bright H II region found in the *WISE* catalog (ID: G345.651+00.015; see also Caswell & Haynes 1987). This source is 55.5″ away from our pointing direction, and thus it overlaps with both the GBT and DSS-43 beams, but not with the *Herschel*/HIFI and PACS observations (see Figure 2). The data at 47″ are a factor of ∼0.2 and ∼0.13 fainter than those observed by the DSS-43 and GBT, respectively, and are thus relatively unaffected by the G345.651+00.015 source. Given that we have [N II] observations at 47″ resolution, we use the 47″ H67α data in our analysis. Note that G345.651+00.015 shows only emission for the component at -8 km s^{-1} (Caswell & Haynes 1987), and thus beam-dilution affects this velocity component only. The emission for the velocity component at -122.8 km s^{-1} appears to be consistent for all observed LOSs, and thus for our analysis we will use the observation at H91α, which has a higher signal-to-noise ratio.

In Figure 9 we show a comparison in a larger number of LOSs between the GBT and DSS-43 observations. Apart from the LOSs discussed above, we find general agreement between observations taken with these two telescopes. All RRLs in the plot are scaled to correspond to the intensity of the H89α line.

We studied the effects of applying the beam-dilution correction to our data as described above. By using the factors derived from 16″ to 47″ using the *Herschel*/PACS data and those from 47″ to 84″ and 115″ using the *WISE* 22 μm observations, we find that the derived electron densities vary by ∼15% for sources observed in RRLs at 84″ and by ∼36% for sources observed at 115″.

Appendix B
Gaussian Decomposition

In Table 6, we show central velocities, FWHM, and peak intensity resulting from the Gaussian decomposition to our RRL and [N II] 205 μm observations. Integrated intensities are listed in Table 1.

Table 6
RRL and [N II] Gaussian Decomposition

LOS	Velocity (km s^{-1})	FWHM (km s^{-1})	$T_{\rm mb}^{\rm RRL}$ (10^{-3} K)
H89α			
G305.1+0.0	−33.2 ± 0.2	23.3 ± 0.5	63.6 ± 3.6
G316.6+0.0	−6.4 ± 1.3	24.2 ± 2.8	4.7 ± 0.7
G316.6+0.0	−48.1 ± 0.6	27.6 ± 1.5	19.5 ± 1.8
G337.0+0.0	−121.5 ± 0.5	19.0 ± 1.3	55.6 ± 5.5
G337.0+0.0	−76.6 ± 0.8	28.3 ± 2.2	43.3 ± 5.5
G342.2+0.0	−131.2 ± 0.6	15.4 ± 1.2	18.5 ± 3.4
G345.7+0.0	−122.8 ± 0.0	23.2 ± 6.8	14.0 ± 1.1
G345.7+0.0	−10.2 ± 0.1	32.2 ± 0.2	61.5 ± 1.1
G349.1+0.0	17.1 ± 0.3	20.2 ± 0.7	104.5 ± 11.4
G349.1+0.0	−93.4 ± 1.3	25.0 ± 2.7	27.7 ± 11.4
H89α			
G349.1+0.0	17.0 ± 0.1	23.2 ± 0.1	131.8 ± 2.9
G349.1+0.0	−91.1 ± 0.1	24.7 ± 0.3	25.3 ± 2.9
G000.0+0.0	−60.5[a]	29.6 ± 0.1	120.9 ± 4.0
G000.0+0.0	−37.1[a]	44.1 ± 0.4	51.1 ± 4.0
G000.0+0.0	12.8[a]	40.3 ± 0.5	31.1 ± 4.0
G000.0+0.0	95.0[a]	29.5 ± 0.4	22.2 ± 4.0
G013.9+0.0	45.5[a]	21.2 ± 0.7	6.1 ± 2.3
G013.9+0.0	30.3[a]	19.1 ± 0.3	24.3 ± 2.3
G030.0+0.0	95.4 ± 0.9	23.3 ± 0.5	15.3 ± 2.5
G031.3+0.0	100.4 ± 0.1	19.2 ± 0.2	31.0 ± 2.3
G031.3+0.0	38.0 ± 0.3	47.7 ± 0.7	10.0 ± 2.3
G049.1+0.0	59.7 ± 0.3	18.9 ± 0.6	6.6 ± 1.1
H67α			
G345.7+0.0	−8.2 ± 1.2	23.8 ± 2.7	35.05 ± 7.3
H54α			
G000.0+0.0	−62.9 ± 1.2	28.8 ± 3.3	24.2 ± 5
[N II]			(K)
G305.1+0.0	−31.6 ± 0.3	22.3 ± 0.6	1.6 ± 0.1
G316.6+0.0	−46.4 ± 0.2	16.6 ± 0.4	1.2 ± 0.1
G316.6+0.0	−6.6 ± 1.4	20.8 ± 2.6	0.2 ± 0.1
G337.0+0.0	−121.8 ± 0.1	9.3 ± 0.2	2.5 ± 0.1
G337.0+0.0	−73.5 ± 0.7	23.2 ± 2.3	0.9 ± 0.1
G342.2+0.0	−130.0 ± 0.4	12.8 ± 0.9	0.7 ± 0.1
G345.7+0.0	−121.0 ± 0.2	6.9 ± 0.6	0.8 ± 0.1
G345.7+0.0	−14.9 ± 0.3	15.6 ± 0.8	1.0 ± 0.1
G349.1+0.0	−84.4 ± 0.6	16.2 ± 1.9	0.7 ± 0.1
G349.1+0.0	14.2 ± 0.2	12.4 ± 0.5	1.7 ± 0.1
G000.0+0.0	−60.5 ± 0.2	15.6 ± 0.6	2.0 ± 0.1
G000.0+0.0	−37.1 ± 2.4	58.9 ± 3.7	0.7 ± 0.1
G000.0+0.0	12.8 ± 1.4	28.3 ± 3.6	0.4 ± 0.1
G000.0+0.0	50.5 ± 1.3	19.2 ± 2.9	0.3 ± 0.1
G000.0+0.0	95.0 ± 1.0	42.4 ± 1.0	0.3 ± 0.1
G013.9+0.0	30.2 ± 0.6	6.3 ± 1.0	0.2 ± 0.1
G013.9+0.0	45.3 ± 0.5	7.9 ± 1.0	0.3 ± 0.1
G030.0+0.0	96.1 ± 0.4	10.4 ± 0.9	0.9 ± 0.1
G031.3+0.0	101.2 ± 0.4	13.9 ± 0.8	1.4 ± 0.1
G031.3+0.0	40.0 ± 2.9	18.7 ± 6.7	0.1 ± 0.1
G049.1+0.0	57.8 ± 0.3	7.8 ± 0.9	0.4 ± 0.1

Note.
[a] The RRL Gaussian fit was done with fixed velocities that were derived from the Gaussian fit to the [N II] spectrum.

ORCID iDs

Jorge L. Pineda https://orcid.org/0000-0001-8898-2800
Loren D. Anderson https://orcid.org/0000-0001-8800-1793
Matteo Luisi https://orcid.org/0000-0001-8061-216X
Paul F. Goldsmith https://orcid.org/0000-0002-6622-8396
Thomas B. H. Kuiper https://orcid.org/0000-0003-1798-4918

References

Akritas, M. G., & Bershady, M. A. 1996, ApJ, 470, 706
Alves, M. I. R., Calabretta, M., Davies, R. D., et al. 2015, MNRAS, 450, 2025
Anderson, L. D., Bania, T. M., Balser, D. S., et al. 2014, ApJS, 212, 1
Anderson, L. D., Bania, T. M., Balser, D. S., & Rood, R. T. 2011, ApJS, 194, 32
Andrievsky, S. M., Martin, R. P., Kovtyukh, V. V., Korotin, S. A., & Lépine, J. R. D. 2016, MNRAS, 461, 4256
Balser, D. S. 2006, AJ, 132, 2326
Balser, D. S., Rood, R. T., Bania, T. M., & Anderson, L. D. 2011, ApJ, 738, 27
Balser, D. S., Wenger, T. V., Anderson, L. D., & Bania, T. M. 2015, ApJ, 806, 199
Bania, T., Wenger, T., Balser, D., & Anderson, L. 2014, Tmbidl V8.0, Zenodo Software Release, 2014 doi:10.5281/zenodo.32790
Bania, T., Wenger, T., Balser, D., & Anderson, L. 2016, TMBIDL: Single dish radio astronomy data reduction package, Astrophysics Source Code Library, doi:10.5281/zenodo.32790
Bania, T. M., Anderson, L. D., Balser, D. S., & Rood, R. T. 2010, ApJL, 718, L106
Bennett, C. L., Fixsen, D. J., Hinshaw, G., et al. 1994, ApJ, 434, 587
Beuther, H., Bihr, S., Rugel, M., et al. 2016, A&A, 595, A32
Brocklehurst, M., & Seaton, M. J. 1972, MNRAS, 157, 179
Brown, R. L., Lockman, F. J., & Knapp, G. R. 1978, ARA&A, 16, 445
Caswell, J. L., & Haynes, R. F. 1987, A&A, 171, 261
Churchwell, E. 2002, ARA&A, 40, 27
Cordes, J. M., & Lazio, T. J. W. 2002, arXiv:astro-ph/0207156
de Graauw, T., Helmich, F. P., Phillips, T. G., et al. 2010, A&A, 518, L6
Esteban, C., & García-Rojas, J. 2018, MNRAS, 478, 2315
Geyer, M., & Walker, M. A. 2018, MNRAS, 481, 1609
Goldsmith, P. F., Langer, W. D., Pineda, J. L., & Velusamy, T. 2012, ApJS, 203, 13
Goldsmith, P. F., Yıldız, U. A., Langer, W. D., & Pineda, J. L. 2015, ApJ, 814, 133
Gordon, M. A., & Sorochenko, R. L. (ed.) 2002, Radio Recombination Lines. Their Physics and Astronomical Applications, Vol. 282 (Dordrecht: Springer)
Haffner, L. M., Dettmar, R.-J., Beckman, J. E., et al. 2009, RvMP, 81, 969
Handa, T., Sofue, Y., Nakai, N., Hirabayashi, H., & Inoue, M. 1987, PASJ, 39, 709
Haverkorn, M., Gaensler, B. M., McClure-Griffiths, N. M., Dickey, J. M., & Green, A. J. 2006, ApJS, 167, 230
Hayden, M. R., Holtzman, J. A., Bovy, J., et al. 2014, AJ, 147, 116
Haynes, R. F., Caswell, J. L., & Simons, L. W. J. 1978, AuJPA, 45, 1
Helfand, D. J., Becker, R. H., White, R. L., Fallon, A., & Tuttle, S. 2006, AJ, 131, 2525
Henshaw, J. D., Longmore, S. N., Kruijssen, J. M. D., et al. 2016, MNRAS, 457, 2675
Hopkins, P. F., Kereš, D., Oñorbe, J., et al. 2014, MNRAS, 445, 581
Johnson, J. A. 2019, Sci, 363, 474
Kurtz, S. 2005, in IAU Symp. 227, Massive Star Birth: A Crossroads of Astrophysics, ed. R. Cesaroni et al. (Cambridge: Cambridge Univ. Press), 111
Langer, W. D., Goldsmith, P. F., Pineda, J. L., et al. 2015, A&A, 576, A1
Langer, W. D., Goldsmith, P. F., & Pineda, J. L. 2016, A&A, 590, A43
Langer, W. D., Velusamy, T., Goldsmith, P. F., et al. 2017a, A&A, 607, A59
Langer, W. D., Velusamy, T., Morris, M. R., Goldsmith, P. F., & Pineda, J. L. 2017b, A&A, 599, A136
Langer, W. D., Velusamy, T., Pineda, J. L., et al. 2010, A&A, 521, L17
Law, C. J., Yusef-Zadeh, F., Cotton, W. D., & Maddalena, R. J. 2008, ApJS, 177, 255
Luisi, M., Anderson, L. D., Balser, D. S., Bania, T. M., & Wenger, T. V. 2016, ApJ, 824, 125
Luisi, M., Anderson, L. D., Balser, D. S., Wenger, T. V., & Bania, T. M. 2017, ApJ, 849, 117
Luisi, M., Anderson, L. D., Liu, B., Anish Roshi, D., & Churchwell, E. 2019, ApJS, 241, 2
Martin, R. P., Andrievsky, S. M., Kovtyukh, V. V., et al. 2015, MNRAS, 449, 4071
Murphy, T., Mauch, T., Green, A., et al. 2007, MNRAS, 382, 382
Persic, M., Salucci, P., & Stel, F. 1996, MNRAS, 281, 27
Persson, C. M., Gerin, M., Mookerjea, B., et al. 2014, A&A, 568, A37
Pety, J. 2005, in Proc. of Annual Meeting of the French Society of Astronomy and Astrophysics, ed. F. Casoli, (Les Ulis: EDP), 721
Pilbratt, G. L., Riedinger, J. R., Passvogel, T., et al. 2010, A&A, 518, L1
Pineda, J. L., Langer, W. D., Goldsmith, P. F., et al. 2017, ApJ, 839, 107
Pineda, J. L., Langer, W. D., Velusamy, T., & Goldsmith, P. F. 2013, A&A, 554, A103
Quireza, C., Rood, R. T., Balser, D. S., & Bania, T. M. 2006, ApJS, 165, 338
Reich, W., Fuerst, E., Haslam, C. G. T., Steffen, P., & Reif, K. 1984, A&AS, 58, 197
Reid, M. J., Menten, K. M., Brunthaler, A., et al. 2014, ApJ, 783, 130
Roelfsema, P. R., Helmich, F. P., Teyssier, D., et al. 2012, A&A, 537, A17
Rohlfs, K., & Wilson, T. L. 2004, in Tools of Radio Astronomy, ed. K. Rohlfs & T. L. Wilson (4th ed.; Berlin: Springer)
Röllig, M., Simon, R., Güsten, R., et al. 2016, A&A, 591, A33
Simpson, J. P., Colgan, S. W. J., Rubin, R. H., Erickson, E. F., & Haas, M. R. 1995, ApJ, 444, 721
Simpson, J. P., Rubin, R. H., Colgan, S. W. J., Erickson, E. F., & Haas, M. R. 2004, ApJ, 611, 338
Wenger, T. V., Balser, D. S., Anderson, L. D., & Bania, T. M. 2018, ApJ, 856, 52
Wenger, T. V., Dickey, J. M., Jordan, C. H., et al. 2019, ApJS, 240, 24